Computation of the Mid-Sagittal Plane in 3D Brain Images

Sylvain Prima, Sébastien Ourselin, Nicholas Ayache

Computation of the Mid-Sagittal Plane in 3D Brain Images

Sylvain Prima, Sébastien Ourselin, and Nicholas Ayache

Abstract— **We present a new method to automatically compute, reorient and recenter the mid-sagittal plane in anatomical and functional 3D brain images. This iterative approach is composed of two steps. At first, given an initial guess of the mid-sagittal plane (generally, the central plane of the image grid), the computation of local similarity measures between the two sides of the head allows to identify homologous anatomical structures or functional areas, by way of a block matching procedure. The output is a set of point-to-point correspondences: the centers of homologous blocks. Subsequently, we define the mid-sagittal plane as the one best superposing the points on one side and their counterparts on the other side by reflective symmetry. Practically, the computation of the parameters characterizing the plane is performed by a least trimmed squares estimation. Then, the estimated plane is aligned with the center of the image grid, and the whole process is iterated until convergence. The robust estimation technique we use allows normal or abnormal asymmetrical structures or areas to be treated as outliers, and the plane to be mainly computed from the underlying gross symmetry of the brain. The algorithm is fast and accurate, even for strongly tilted heads, and even in presence of high acquisition noise and bias field, as shown on a large set of synthetic data. The algorithm has also been visually evaluated on a large set of real MR images. We present a few results on isotropic as well as anisotropic anatomical (MR, CT) and functional (SPECT, PET) real images, for normal and pathological subjects.**

Keywords— **Magnetic Resonance Imaging, Symmetry, Mid-Sagittal Plane**

I. Introduction

A. Presentation of the problem

A NORMAL human head exhibits a rough bilateral symmetry. What is easily observable for external structures (ears, eyes, nose, skull...) remains valuable for the brain and its components. It is split into two hemispheres, in which each substructure has a counterpart of approximately the same shape and location on the opposite side (temporal, frontal, occipital lobes, ventricles...). The hemispheres are interconnected by commissural fibers, most of which are found in the *corpus callosum*.

However, conspicuous morphological differences between the hemispheres make the brain systematically asymmetrical. Notably, in most cases, the right frontal and left occipital lobes are larger than their respective counterparts, as if the brain was subjected to a torque around its anteroposterior axis (see Figure 1) [1]. More subtly, the natural variability of the cortex translates into slight differences between hemispheres. In the same way, cerebral lateralization has been largely demonstrated since the works of Paul Broca (1861) and Carl Wernicke (1874). For example, the left hemisphere is generally dominant for linguistic functions, and traditionally viewed as "analytical", whereas the right one is specialized for non-verbal tasks such as visual perception or spatial orientation, and considered as "synthetic".

The question of whether the anatomical and functional brain asymmetries relate to each other remains debatable to the point, but close connections are suspected. In particular, *post mortem* [2] as well as MR [3] studies have reported a correlation between left-hemispheric dominance for language, right-handedness and a larger left *planum temporale*; the latter lies within the Wernicke's area, which is known to be involved in comprehension of spoken or written language. However, this relation does not always hold and there exist numerous exceptions. In the same way, the brain torque is thought to be linked to handedness and gender [4]. These works suggest that symmetry considerations are key to the understanding of cerebral functioning.

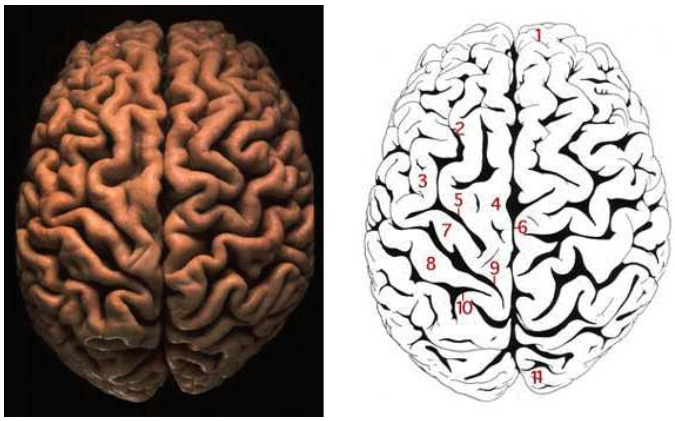

Fig. 1. **The brain torque.** The right frontal lobe (1) is larger than the left one, and this is the opposite for the occipital lobe (11). Description of the hemispheres: 1. Frontal pole 2. Superior frontal sulcus 3. Middle frontal gyrus 4. Superior frontal gyrus 5. Precentral sulcus 6. Longitudinal cerebral fissure 7. Precentral gyrus 8. Postcentral gyrus 9. Central sulcus 10. Postcentral sulcus 11. Occipital pole. This illustration comes from the Virtual Hospital [5].

Volumetric medical images convey information about anatomical (MR, CT...) or functional (PET, SPECT...) symmetries and asymmetries, which is usually hidden by the tilt of the patient's head in the device during the scanning process. This makes visual inspection or analysis harder, because the homologous anatomical structures or functional areas in both hemispheres are not displayed in

S. Prima, S. Ourselin and N. Ayache are with the Epidaure Project, INRIA, 2004 route des Lucioles, BP 93, 06902 Sophia Antipolis, France. Sylvain Prima is also currently with the McConnell Brain Imaging Centre, Montreal Neurological Institute, McGill University, Montreal, Quebec, Canada H3A 2B4. E-mails: prima@bic.mni.mcgill.ca, {sprima,sourseli,na}@sophia.inria.fr.

the same axial or coronal slice of the 3D image. The correction of this tilt is of great interest for many tasks, allowing normal (torque effect, intrinsic variability...) as well as abnormal (unilateral pathologies...) departures from symmetry to appear more clearly. This helps comparing the two sides of the brain by making manual or automatic measurements easier.

It can be helpful for diagnosis in many cases: fractures in CT images, lesions or bleedings in MR images, defaults of perfusion in SPECT images... Recent studies suggest the detection of bilaterally increased pulvinar signal as a test for diagnosing the variant Creutzfeldt-Jakob disease in T2-weighted MR images [6], [7]. Identically, bilateral reduction of metabolic activity in parietal, temporal, and prefrontal regions is known to be an important feature for diagnosing the Alzheimer's disease [8]. Some other pathologies are thought to be strongly linked with abnormalities of brain asymmetry: the reduction of the *planum temporale* asymmetry in dyslexic [9] as well as schizophrenic [10] patients has been reported; for the latter, a loss of brain torque is also suspected [11], [12].

Correcting the tilt of the head is equivalent to defining and computing a proper plane to split it into two roughly identical parts, and then realigning this plane, often qualified as *mid-sagittal*, with the center of the image lattice, for a better display of the whole 3D volume. Note that, in the following, we use the word "tilt" as referring to both the "misalignment" and the "miscentering" of the plane. This mid-sagittal plane can be the basis for further symmetry analyses. Marais *et al.* compute the distances between the cortical surface of the hemispheres and the mid-sagittal plane; these measures provide a quantitative 2D symmetry map [13]. In previous works, we compute a dense 3D field over the whole volume, that matches the head and its reflection with respect to the mid-sagittal plane [14], [15]. This field conveys the head and brain symmetry: in particular, it is null where there is perfect symmetry, *i.e.*, when no deformation is needed to transform one structure into its counterpart.

Several papers have previously considered the problem of computing the mid-sagittal plane in head images. There are mainly two classes of methods, differing in their definition of the searched plane, which can be either the plane best matching the cerebral interhemispheric fissure, or the plane maximizing a symmetry criterion, *i.e.*, making the two parts of the head lying on each side most similar. In the following, we detail the advantages and drawbacks of these two approaches, and summarize their main features and applications in Table I.

Methods	Based on...	Applications
[16]	fissure	MR
[13]	fissure	MR
[17]	symmetry	MR, PET
[18]	symmetry	MR, CT, PET, SPECT
[19]	symmetry	MR, CT
[20], [21]	symmetry	MR, CT
[22]	symmetry	PET, SPECT
[23]	symmetry	PET

TABLE I
SUMMARY OF THE MAIN FEATURES OF EXISTING METHODS.

B. State of the art

B.1 Methods based on the interhemispheric fissure

Hypotheses. The basic and simple hypotheses underlying these methods are that the interhemispheric fissure of the brain is roughly planar, and that it provides a good landmark for further volumetric symmetry analysis.

Methods. Generally, the fissure is segmented in MR images. Marais *et al.* extract it slice-by-slice using snakes [13]. Then, a 3D plane is found, using an orthogonal regression from a set of control points representing the segmented curve. Brummer proposes a 3D extension of the Hough transform principle to estimate the mid-sagittal plane [16]. A Hough transform is computed on each 2D coronal slice to detect straight lines. The accumulator cells of the transform contain the magnitude of the gradient computed in 3D. After these 2D lines are extracted, simple geometrical considerations show how to robustly compute the 3D plane from these lines. As a preprocessing, the head must be segmented to avoid detecting meaningless lines.

Advantages & Drawbacks. As these approaches focus on the interhemispheric fissure, the resulting reorientation and recentering of the head is insensitive to strong asymmetries, provided there is not a mass effect near the fissure. Conversely, as the global symmetry of the whole brain is not considered, the resulting algorithms are very sensitive to the often observed curvature of the fissure, mainly due to the brain torque (see Figure 1), which can lead to a meaningless plane. For example, the method of Marais *et al.* only relies on a few points representing the snakes [13], and the orthogonal regression is known not to be robust with respect to outliers; the intrinsic curvature of the fissure and the potential errors of segmentation can strongly corrupt the result. In addition, the Hough transform principle [16] will fail to detect lines if the hypothesis of weak curvature is violated. At last, these methods are not adaptable to other modalities, such as CT, PET or SPECT (see Figures 20, 21 and 22), where the fissure is not clearly visible.

B.2 Methods based on a symmetry criterion

Hypotheses. There are relatively simple methods for finding a plane of reflective symmetry in the case of perfectly symmetrical geometrical objects, in 2D or 3D. In this case, it can be demonstrated that any symmetry plane of a body is perpendicular to a principal axis of inertia. In the case of medical images, the problem is different, because normal and abnormal asymmetries modify the underlying symmetry of the brain: a perfect symmetry plane does not exist. To tackle this problem, an intuitive idea is to define the mid-sagittal plane as the one that maximizes the

similarity (to be defined later) between the brain and its reflection, *i.e.*, the plane with respect to which the brain exhibits maximum symmetry. Practically, this approximate symmetry plane is close to the fissure, but is computed using the whole 3D image and no anatomical landmarks.

Methods. Most of these methods share a common general scheme. First, an adequate parameterization is chosen to characterize any plane of the 3D Euclidian space by a vector composed of a few coefficients. Then, a search is completed over the set of possible planes to achieve the maximum of an adapted similarity measure between the original image and its reflection.

The chosen criterion is often the cross correlation between the intensities of the two 3D images [17]. A slightly different approach is presented by Liu *et al.* [20], who estimate a 2D mid-sagittal axis for each coronal or axial slice, and then deduce a 3D plane from the set of these lines, following geometrical considerations as Brummer [16]. For a given slice, the selected axis is the line that maximizes the cross correlation between the two reflected images with respect to this line. The main drawback of this method is that when the head is strongly tilted, the homologous anatomical structures or functional areas in both hemispheres are not displayed in the same coronal or axial slices: the computed mid-sagittal lines are then likely to be meaningless. The method described by Junck *et al.* [22] is basically the same, but limited to 2D axial slices (no 3D plane is computed), and applied to other modalities (see Table I for details).

Instead of intensities, the criterion can be computed from features derived from the original image. Liu *et al.* [21] estimate the mid-sagittal plane from an edge image rather than the original gray level volume, following the maximization scheme they previously proposed [20]. Sun and Sherrah [24], [19] compute the gradient orientation histogram whose values are reported on a tessellated unit sphere, yielding the Extended Gaussian Image (EGI). In theory, if the brain is symmetrical, so is its EGI. The direction of the mid-sagittal plane is the one that maximizes the cross correlation between the EGI and its reflection with respect to this plane, within the discrete set of orientations defined by the tessellation. As a preprocessing step, the image is rotated and centered according to the principal axes of inertia and the center of mass of the head. The resolution is limited to the tessellation of the unit sphere, and to well contrasted images (CT and MR), because of the use of the gradient.

Contrary to the first class of methods (Section I-B.1), the whole 3D volume is taken into account, which means that the overall gross symmetry of the brain is used. Consequently, these methods are much less sensitive to the variability of the interhemispheric fissure and its curved shape. The trade-off is the need for the similarity measure to be robust with respect to departures from the gross underlying symmetry, *i.e.*, the normal and pathological asymmetries of the brain. This robustness is difficult to achieve with global criteria such as the cross correlation, that is affected in the same way by areas in strong (*i.e.*, symmetrical) and weak (*i.e.*, asymmetrical) correlation. In practice, the latter can severely bias the estimation of the plane [17].

To overcome this issue, another similarity criterion is proposed by Minoshima *et al.* [23]: the stochastic sign change, previously shown to be efficient in the case of rigid registration, even for quite dissimilar images [25], [26]. In the same way, a new symmetry measure introduced by Smith and Jenkinson allows to mainly take into account strongly symmetrical parts of the brain [18]. First, an optimal plane is computed within the set of planes sharing the same normal vector: for each line with this orientation in the image, a center of symmetry is identified in its intensity profile, by maximization of a criterion which is equal to 1 (resp. -1) in case of perfect symmetry (resp. antisymmetry). The plane best fitting the set of centers and a symmetry criterion attached are subsequently derived, giving more strength to centers with respect to which the lines exhibit strong symmetry. The mid-sagittal plane is the plane yielding the maximum symmetry criterion among all the possible orientations.

Advantages & Drawbacks. Apart from their sensitivity to asymmetries, another common drawback of these methods is the computational cost of the related algorithms, mainly due to the optimization scheme when exploring the set of possible planes. However, this cost can be often reduced: the discretization of the parameters space (that limits the accuracy of the results) or a prior knowledge about the position of the optimal plane allow to investigate only a limited number of planes. Thus, the reorientation of the principal axes of inertia of the head and the centering of its center of mass is often a useful preprocessing step. A multi-resolution scheme can also accelerate the process [17]. Finally, compared to the methods based on the interhemispheric fissure, a significant advantage of most of these approaches is their ability to tackle other modalities than MR, in particular functional images: results on CT, PET, and SPECT images are presented in the referred papers.

C. Overview of the article

In this article, we present a new symmetry-based method to automatically compute, reorient and recenter the mid-sagittal plane in anatomical and functional images of the brain. This method, generalizing an approach we previously described [14], [15], is an iterative process composed of two steps. At first, given an initial guess of the mid-sagittal plane (generally, the central plane of the image grid), the computation of local rather than global similarity measures between the two sides of the head allows to identify homologous anatomical structures or functional areas, using a block matching procedure. The output is a set of point-to-point correspondences: the centers of homologous blocks. Subsequently, we define the mid-sagittal plane as the one best superposing the points on one side and their counterparts on the other side by reflective symmetry. Practically, the computation of the parameters characterizing the plane is performed by a least trimmed squares

estimation. Then, the estimated plane is aligned with the center of the image grid, and the whole process is iterated until convergence.

This approach deals with two severe drawbacks of classical symmetry-based methods. First, the computation of local measures of symmetry and the use of a robust estimation technique [27] allow to discriminate between symmetrical and asymmetrical parts of the brain, the latter being naturally treated as outliers. Consequently, the computation of the mid-sagittal plane mainly relies on the underlying gross symmetry of the brain. Second, the regression step yields an analytical solution, computationally less expensive than the maximization of the global similarity measures described in Section I-B.2.

We describe this new approach in Section II. In Section III, we show that we are able to cope with strongly asymmetrical and tilted head or brain, even in presence of acquisition noise and bias field, with very high accuracy and low computation time. In Section IV, we present results on real anatomical (MR, CT) and functional (PET, SPECT) images.

II. Description of the method

A. Presentation of the main principles

As an introduction, we recall the principle of the method we presented in a previous work [14], [15]. Given I, an MR image of the head, the mid-sagittal plane P is defined as the one best superposing the points $\{a_i\}$ and $\{S_P(a_i'')\}$, where a_i is a head voxel, a_i'' its anatomical counterpart on the other side, and S_P the symmetry with respect to the searched plane P. Practically, P is obtained by minimization of the least squares (LS) criterion $\sum_i \|a_i - S_P(a_i'')\|^2$, where $\|.\|$ is the Euclidian norm. An analytical solution of this problem is described in Appendix 1. The pairs $\{(a_i, a_i'')\}$ are obtained as follows (see also Figures 2 and 3):

- The original image I is flipped with respect to an arbitrary plane K, yielding the image $S_K(I)$ (S_K is the symmetry with respect to K).
- The "demons" algorithm [28] finds the anatomical counterpart a_i' in $S_K(I)$ of each point a_i in I, by way of a non-rigid registration between the two images.
- $a_i'' = S_K(a_i')$ is the anatomical counterpart of a_i on the other side of the head. For example, in I, the point a_i, located in the right temporal lobe (radiological conventions) is matched with the point a_i'', located in the left temporal lobe (see Figure 2).

Experimentally, we observed that the quality of registration between I and $S_K(I)$ is equivalent for a large set of planes K, provided they are not "too far" from the search mid-sagittal plane P; this means that the set of points $\{a_i''\}$ is independent of the chosen plane K. Practically, the most reasonable and simple choice for K is the plane located at the center of the image lattice, which is likely to be relatively close to P.

Once P is computed, the transformation $R = S_K \circ S_P$ is a rotation if P and K are not parallel and a translation if P and K are parallel. The transformation $R^{1/2}$, when applied to the image I, automatically aligns the plane P with K, the latter being considered as fixed to the image grid (see Appendix 2). Several difficulties and limitations arise when using this method:

- As many of the classical symmetry-based methods, normal and pathological asymmetries can severely degrade the computation of the plane. Even though it is based on local instead of global measures of symmetry, the LS minimization is not robust with respect to outliers [27], and will be strongly affected by the departures from the underlying symmetry.
- In particular, the non-rigid registration algorithm will provide aberrant matchings when a structure is absent in one hemisphere (a lesion, one track of white matter...), or when two structures are present but too different from each other. These failures are difficult to detect, and will affect the quality of the registration in the neighborhood, because the field is smoothed to ensure its spatial coherence. These meaningless correspondences can significantly degrade the LS criterion and its subsequent minimization.
- At last, the "demons" algorithm mainly relies on the gradient of the image, and proved to be efficient mainly for low-textured images like MR or CT. Consequently, this approach is difficult to extend to functional images such as SPECT or PET.

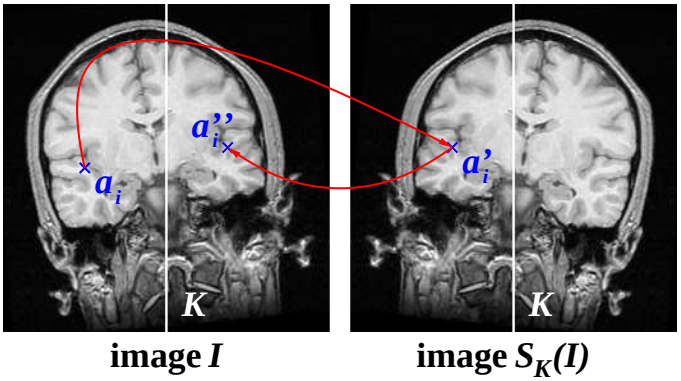

Fig. 2. **The non-rigid registration strategy.** Left: coronal slice of the original image I, with K, the central plane of the grid, drawn in white. Right: $S_K(I)$ is the same image as I, but flipped with respect to K. The point a_i in I is matched with the point a_i' in $S_K(I)$; $a_i'' = S_K(a_i')$ is a point of I, counterpart of a_i on the other side of the head.

B. Modification based on a block matching strategy and a robust estimation technique

We propose a modification of this approach, allowing to compute the mid-sagittal plane mainly from very symmetrical structures or areas, and to tackle both functional and anatomical images. The new algorithm partly rests on a block matching procedure. This technique was initially developed for video compression [29], and has inspired several algorithms of non-rigid [30], [31] as well as 2D [32] and 3D [33] rigid registration. In this last case, the principle is to compute a displacement field between the reference image I and the current floating image $T(J)$ *via* a block matching strategy, to gather these displacements to estimate a rigid

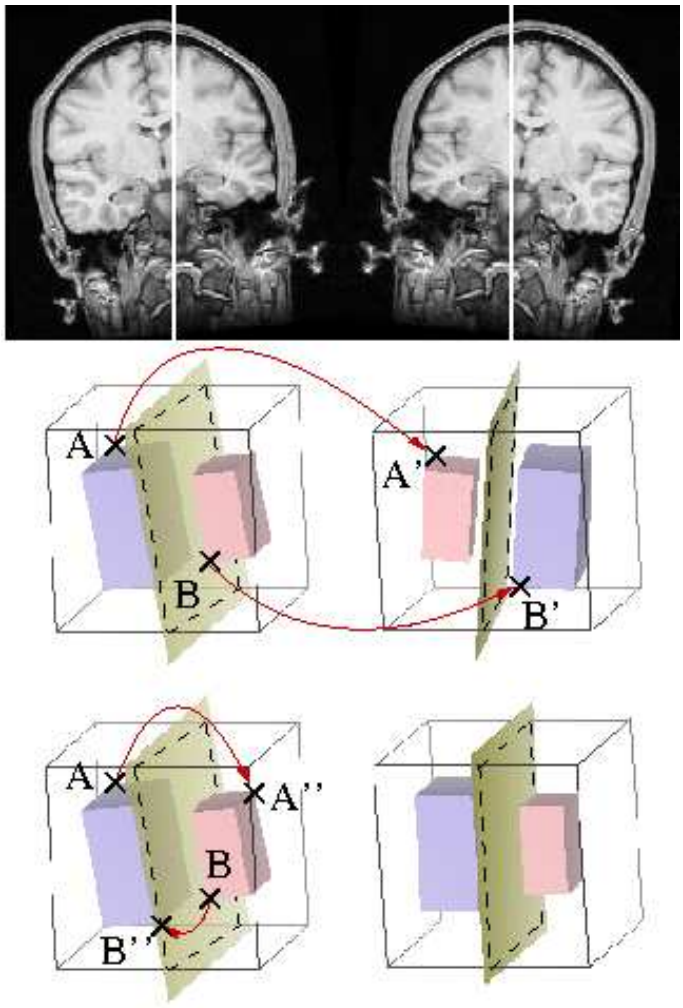

Fig. 3. **Schematic principle of the non-rigid registration strategy.** Top panel: coronal slices of I and $S_K(I)$ (in radiological conventions), K being the central plane of the image grid. Middle panel: schematic versions of I and $S_K(I)$. The searched mid-sagittal plane is drawn between them. In $S_K(I)$, the small (resp. big) parallelepiped is a virtual right (resp. left) hemisphere. The registration between I and $S_K(I)$ gives pairs of corresponding points (A, A'), (B, B'),... Bottom panel: $A'' = S_K(A')$ and $B'' = S_K(B')$ are points of I, homologous of A and B in the other hemisphere. The plane P minimizing $\sum_i (S_P(A''_i) - A_i)^2$ is the mid-sagittal plane, which is then aligned with the center of the image grid.

transformation R, and to update the current transformation according to $T \leftarrow R \circ T$. The whole process is initiated with $T = Id$, and is iterated until convergence. The idea motivating an iterative scheme is that the better the matching, the better the transformation, and conversely.

In this article, we adapt this methodology to the computation of the mid-sagittal plane in a 3D image I. First, we compute a displacement field between I and $S_U(I)$ *via* a block matching strategy, given the current mid-sagittal plane U. Second, we gather these displacements to compute a new mid-sagittal plane Q, by way of a least trimmed squares (LTS) estimation. Third, we update the current mid-sagittal plane: $U \leftarrow Q$. The whole process is initiated with $U = K$, the central plane of the image grid, and is iterated until convergence. Contrary to the approach based on the demons algorithm, the quality of the matching is highly dependent on the current mid-sagittal plane U (see Figure 5), which motivates an iterative scheme.

Practically, for algorithmic reasons, we implemented the method in a slightly different, but equivalent way. At each iteration, we realign the newly estimated plane with the center of the image grid; consequently, the plane K, fixed to the center of the grid, is the current mid-sagittal plane throughout the process, which can then be rewritten (see also Figure 6):

- Step 1: initialization: $R = Id$
- Step 2: computation of a displacement field between $R(I)$ and $S_K \circ R(I)$ *via* a block matching strategy
- Step 3: LTS estimation of the new mid-sagittal plane Q
- If Q and K are "sufficiently close" to each other, the definitive mid-sagittal is $P = Q$; practically, the end condition is $d(Q, K) < 0.1$ voxels (the distance between two planes is defined in Figure 4)
- Else, update $R \leftarrow (S_K \circ S_Q)^{1/2} \circ R$, and go back to Step 2

In the following, we give further details about the block matching (Section II-B.1) and the estimation (Section II-B.2) steps, and explain how this iterative process is encompassed within a multiscale scheme (Section II-B.3).

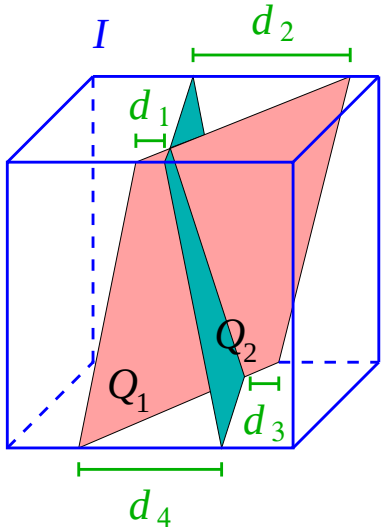

Fig. 4. **Distance between two planes.** We define the distance between two arbitrary planes Q_1 and Q_2, intersecting the four horizontal edges of the image grid, as the maximum $d(Q_1, Q_2)$ of the four distances d_1, d_2, d_3, d_4. This distance is not only used to define an end condition for the process iterating the block matching and the estimation steps, but also for the LTS estimation itself.

B.1 Computation of interhemispheric correspondences by a block matching strategy

At a given iteration, the pairs of correspondences $\{(a_i, a'_i)\}$ are obtained by way of a block matching procedure between the images $R(I)$ and $S_K \circ R(I)$. The common lattice of the two images (of size $X \times Y \times Z$) defines a set of rectangular parallelepipedic blocks of voxels $\{\mathcal{B}\}$ in $R(I)$ and $\{\mathcal{B}'\}$ in $S_K \circ R(I)$, given their size $N_x \times N_y \times N_z$: both

images contain $(X - N_x + 1) \times (Y - N_y + 1) \times (Z - N_z + 1)$ such blocks. We aim at matching each block in $\{\mathcal{B}\}$ with the block in $\{\mathcal{B}'\}$ maximizing a given similarity measure. Practically, it is not computationally feasible to make an exhaustive search within $\{\mathcal{B}'\}$ for each block of $\{\mathcal{B}\}$. In addition, we have an *a priori* knowledge about the position of the correspondent $\mathcal{B}'$ of $\mathcal{B}$: if the head is not too tilted, $\mathcal{B}'$ is to be located in a neighborhood of $\mathcal{B}$. Thus, we constrain the search procedure to subsets by introducing parameters $\Omega = (\Omega_x, \Omega_y, \Omega_z)$, $\Delta = (\Delta_x, \Delta_y, \Delta_z)$, $\Sigma = (\Sigma_x, \Sigma_y, \Sigma_z)$ as follows (see also Figure 5):

- We limit the search for correspondences to one block $\mathcal{B}$ every Δ_x (resp. Δ_y, Δ_z) voxels in the x (resp. y, z) direction, defining a subset of $\{\mathcal{B}\}$; $\Delta = (\Delta_x, \Delta_y, \Delta_z)$ determines the density of the computed displacement field between I and $S_K(I)$
- For each block $\mathcal{B}$ in this subset, we define a sub-image in $S_K(I)$, centered on $\mathcal{B}$, which delimits a neighborhood of search. This sub-image is composed of the voxels in $S_K(I)$ located within a distance of Ω_x (resp. Ω_y, Ω_z) voxels in the x (resp. y, z) direction from $\mathcal{B}$. This yields a rectangular parallelepipedic sub-image of size $(N_x + 2\Omega_x) \times (N_y + 2\Omega_y) \times (N_z + 2\Omega_z)$ in $S_K(I)$, which contains $(2\Omega_x + 1) \times (2\Omega_y + 1) \times (2\Omega_z + 1)$ blocks $\mathcal{B}'$ (provided this sub-image is entirely located in $S_K(I)$)
- In this sub-image, we examine one block $\mathcal{B}'$ every Σ_x (resp. Σ_y, Σ_z) voxels in the x (resp. y, z) direction; $\Sigma = (\Sigma_x, \Sigma_y, \Sigma_z)$ determines the resolution of the displacement field

The output of the block matching procedure is a series of pairs of correspondences (a_i, a_i') between $R(I)$ and $S_K \circ R(I)$, a_i and a_i' being the centers of matched blocks. These pairs of points form a displacement field between $R(I)$ and $S_K \circ R(I)$, which conveys local information about head symmetry and asymmetry. The points $\{a_i'\}$ are then flipped back with respect to K, giving the points $\{a_i'' = S_K(a_i')\}$. The point a_i'' is the counterpart of a_i on the opposite side of the head (see Figure 5).

Different intensity-based criteria can be chosen as a similarity measure, such as the Correlation Coefficient (CC), also called the normalized cross correlation [34], the Correlation Ratio (CR) [35] or the Mutual Information (MI) [36], [37]. Each of these measures assumes an underlying relationship between the voxel intensities of the two images, respectively affine (CC), functional (CR), or statistical (MI) [38]. Practically, the CR and the MI are well suited to multimodal registration, whereas the CC is suited to monomodal registration. In our case, $R(I)$ and $S_K \circ R(I)$ belong to the same imaging modality: an affine, or locally affine relationship can be assumed, and thus we use the CC, whatever the modality of I. In Section III, we will investigate the validity of this assumption when I is corrupted by a bias field. If we consider a block $\mathcal{B}$ in $R(I)$, with voxels of intensities $x_1, \ldots, x_n$, and a block $\mathcal{B}'$ in $S_K \circ R(I)$, with voxels of intensities $y_1, \ldots, y_n$, the CC between $\mathcal{B}$ and $\mathcal{B}'$ is equal to:

$$\mathrm{CC} = \frac{\frac{1}{n}\sum_{i=1}^{n}(x_i - \bar{x})(y_i - \bar{y})}{\frac{1}{n}\sqrt{\sum_{i=1}^{n}(x_i - \bar{x})^2 \sum_{i=1}^{n}(y_i - \bar{y})^2}} = \frac{\overline{xy} - \bar{x}\bar{y}}{\sigma(x)\sigma(y)}$$

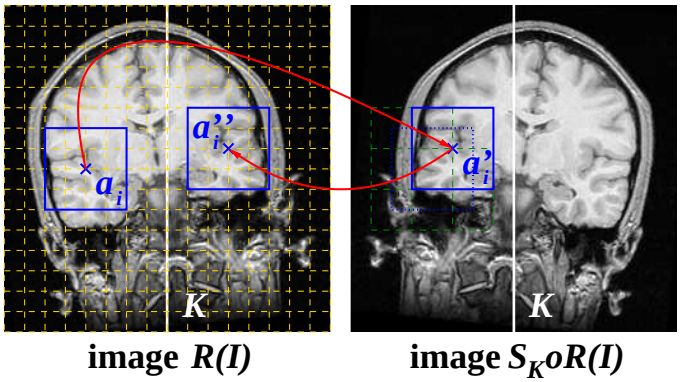

Fig. 5. **The block matching strategy.** We display coronal slices of the brain. The point a_i' in $S_K \circ R(I)$ is homologous to the point a_i in $R(I)$; $a_i'' = S_K(a_i')$ is the counterpart of a_i in the other hemisphere. Here, $R(I)$ and $S_K \circ R(I)$ contain 128^3 voxels, and the chosen parameters are: $N = (32, 32, 32)$, $\Delta = (8, 8, 8)$, $\Omega = (8, 8, 8)$, $\Sigma = (16, 16, 16)$. In $R(I)$, the subset of $\{\mathcal{B}\}$ is defined by the white grid with dashed lines (parameters Δ). Around the black block with solid lines of center a_i, superposed on $S_K \circ R(I)$ (in black with dashed-dotted lines), a neighborhood of search is delimited (parameters Ω). In this sub-image of $S_K \circ R(I)$, the search is completed on the subset of $\{\mathcal{B}'\}$ defined by the white grid with dashed lines (parameters Σ). In this case, for each of the $13^3 = 2197$ such defined blocks in $R(I)$, the search is performed on $2^3 = 8$ blocks in $S_K \circ R(I)$. As noted in the text, the quality of the matching highly depends on the plane K, because the blocks $\{\mathcal{B}\}$ and $\{\mathcal{B}'\}$ have the same orientation. Consequently, even if the brain is perfectly symmetrical, there does not exist any pair of matched blocks in perfect correlation ($|\mathrm{CC}| = 1$) if K is different from the symmetry plane. That motivates an iterative scheme which consists in successive block matching and estimation steps.

It can be easily shown that $-1 \leq \mathrm{CC} \leq 1$. The CC measures the strength of the affine relationship between $\mathcal{B}$ and $\mathcal{B}'$. In particular, if $|\mathrm{CC}|=1$, there exist coefficients α and β such that $y_i = \alpha x_i + \beta$ for all the voxels $i = 1, \ldots, n$ in these blocks. This block matching approach, based on local similarity measures, allows to exclude very asymmetrical and meaningless areas from the computation of the plane. If no block $\mathcal{B}'$ in the subset defined in $S_K \circ R(I)$ exhibits a high $|\mathrm{CC}|$ with a given block $\mathcal{B}$ in the subset defined in $R(I)$, its center is eliminated straightforwardly, by setting a convenient threshold (typically, $|\mathrm{CC}| \leq 0.1$); this was not easily feasible in our former approach [14], [15]. In practice, this happens when the structures existing in one given block in $R(I)$ are absent from any block in $S_K \circ R(I)$, which is the case for strongly asymmetrical areas. This allows also to eliminate the great majority of background voxels. Thus, the estimation step, performed with these preselected interhemispheric correspondences, is mainly based on symmetrical regions. The robust technique we use (a LTS estimation) allows to exclude the remaining asymmetrical areas from the computation of the plane (see Figures 10 and 15 for illustrations of these points on synthetic and real MR images).

B.2 Computation of the mid-sagittal plane by a least trimmed squares estimation

Once the block matching procedure is completed, a LTS estimation is used to find the plane Q best superposing the m points $\{a_i\}$ and their counterparts $\{a_i''\}$ by reflective symmetry. The LTS estimation has been proved to be far more robust to outliers than the classical LS method [27]. Here, noting the residuals $r_i = a_i - S_Q(a_i'')$, it consists in minimizing $\sum_{i=1}^{h} \|r\|_{i:m}^2$ rather than $\sum_{i=1}^{m} \|r_i\|^2$ (LS criterion), where $\|r\|_{1:m} \leq \ldots \leq \|r\|_{m:m}$ are the ordered norms of the residuals and h is an integer close to $m/2$; the LTS estimator then achieves its best robustness properties, and the breakdown point attains 50%, which means that it is able to tackle as much as 50% of outliers. Further discussions about the exact optimal value for h are given by Rousseeuw and Leroy [27].

In our specific problem, we have to deal with two kinds of outlying measures. First, aberrant matchings can be obtained if the head is strongly tilted. Second, even after the initial selection that eliminates blocks with low |CC|, blocks conveying strong asymmetries can remain. This happens when a structure is present on both sides, but at different locations: the two matched blocks containing this structure are likely to exhibit a high |CC|. The use of a robust estimation technique enables the computed plane to be only based on the underlying gross symmetry of the head, the asymmetries being treated as outliers. No explicit solution exists for the computation of the LTS estimate. Following Rousseeuw and Van Driessen [39], we devised an iterative scheme that allows to compute a plane yielding a (at least local) minimum of the criterion:

- Step 1: compute the plane $\tilde{Q}$ minimizing the LS criterion $\sum_{i=1}^{m} \|a_i - S_{\tilde{Q}}(a_i'')\|^2$ (see Appendix 1)
- Step 2: compute the norm of the residuals $\|r_i\| = \|a_i - S_{\tilde{Q}}(a_i'')\|$ for the whole dataset $\{(a_1, a_1''), \ldots, (a_m, a_m'')\}$
- Step 3: sort out the norm of the residuals $\|r_i\|$
- Step 4: recompute the LS estimate $\hat{Q}$ of the mid-sagittal plane on the data that exhibit the residuals with the lowest norms
- If $\hat{Q}$ and $\tilde{Q}$ are "sufficiently close" to each other (see Figure 4), the LTS estimate of the mid-sagittal plane is $Q = \hat{Q}$; practically, the end condition is $d(\tilde{Q}, \hat{Q}) < 0.1$ voxels (see Figure 4)
- Else, update $\tilde{Q} \leftarrow \hat{Q}$, and go back to Step 2

B.3 Multiscale scheme

Given a set of parameters N, Ω, Δ, Σ, the complexity of the block matching process is proportional to $\frac{(N_x N_y N_z)(\Omega_x \Omega_y \Omega_z)}{(\Delta_x \Delta_y \Delta_z)(\Sigma_x \Sigma_y \Sigma_z)}$ [32]. Intuitively, when $R(I)$ is strongly tilted, $R(I)$ and $S_K \circ R(I)$ are very different from each other, and the neighborhood of search must be large (parameters Σ), to deal with strong differences in translation and rotation. In this case, we also expect large windows (parameters N) to give more meaningful CC than small ones. This implies a large computational cost. On the contrary, when $R(I)$ is already well aligned, we can restrict the neighborhood of search, and have more confidence in the CC computed on small windows.

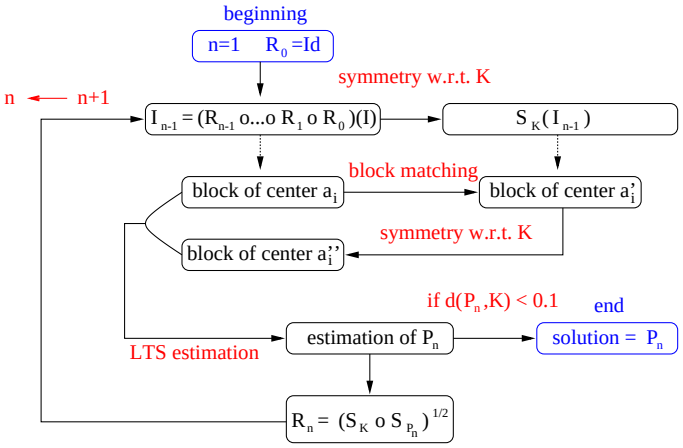

Fig. 6. **General scheme for the computation of P at a given scale.** We describe the iterative process for a given choice of parameters N, Ω, Δ, Σ. The composition of the successively estimated rigid transformations that realign the mid-sagittal plane avoids multiple resampling. The process stops when the distance between two successively computed planes is lower than 0.1 voxels (see Figure 4). Practically, the algorithm converges in about 5 iterations. This whole iterative process is encompassed within a multiscale framework (see Section II-B.3).

Thus, we implemented a multiscale scheme to achieve a good trade-off between accuracy and complexity. Initially, we suspect the head to be strongly tilted, and make a first estimation of the mid-sagittal plane with large values of N, Ω, Δ, Σ, based on a displacement field of low density and low resolution. This estimate P_n^1 is the central plane of $(R_n^1 \circ \ldots \circ R_0^1)(I)$ (n is the number of iterations at a given scale, see Figure 6). Then, we decrease the parameters so that the complexity remains constant, the new estimate P_n^2 is the central plane of $(R_n^2 \circ \ldots \circ R_0^2 \circ R_n^1 \circ \ldots \circ R_0^1)(I)$, and so on. At the last scale, the estimation is based on a displacement field of high density and high resolution, and is likely to be accurate. Practically, we make the following usual choices for isotropic as well as anisotropic images:

- The initial values of the parameters are:
  - $N = ([X/4], [Y/4], [Z/4])$ or $N = ([X/8], [Y/8], [Z/8])$ (discussed in the next section)
  - $\Omega = N$, $\Delta = \Sigma = N/4$
- At each iteration, the parameters are automatically updated as follows:
  $N \leftarrow N/2$, $\Omega \leftarrow \Omega/2$, $\Delta \leftarrow \Delta/2$, $\Sigma \leftarrow \Sigma/2$.
- The updating in the direction x (resp. y, z) stops if a further step would make N_x (resp. N_y, N_z) smaller than 4. At this scale, the small block size makes the computed CC become meaningless. The whole process stops when there is no updating in any direction. For an image of size 128^3 and for each of the 2 choices we usually make for initial parameters, we get 4 and 3 scales respectively, and $\Delta = \Sigma = (1, 1, 1)$ at the last scale: this means that we obtain a displacement field of high density and resolution.

III. Validation on simulated MR images: robustness and accuracy analysis

A. Materials

In this section, we present a series of validation experiments on simulated data, to investigate the robustness and the accuracy of the algorithm. The first objective is to identify the breakdown point of the algorithm, *i.e.*, the maximum tilt of the head below which it is always able to retrieve the mid-sagittal plane with good accuracy. The second objective is to study its behavior when severe asymmetries disturb the underlying symmetry, or when a bias field corrupts the image intensities. These validations aim at identifying a set of optimal initial parameters (see Section II-B.3) for which the algorithm achieves its best properties. For this purpose, we generated a synthetic dataset of 1152 images as follows.

First, a perfectly symmetrical image I_1 is created. We consider an original MR image I with 256^3 voxels of size 0.78mm^3, provided by Dr. Neil Roberts, Magnetic Resonance and Image Analysis Research Centre (University of Liverpool, UK). Running the algorithm directly on high resolution images leads to a prohibitive computation time; we resample I to get a new image of size 128^3. In the latter, a mid-sagittal plane is determined by visual inspection, and matched with the center of the image lattice. One half of the brain is removed, and the other half is flipped with respect to the center of the image grid, which then constitutes a perfect symmetry plane for this new image I_1, and is the ground truth for our validation experiments.

Second, 10 artificial spherical lesions with different gray levels (from 100 to 130) and radiuses between 5 and 10 voxels are added inside the brain at different locations, to simulate strong focal "abnormal" asymmetries. Moreover, 5 local spherical expansions and shrinkings are applied (notably in the frontal, occipital and temporal lobes), that significantly affect the neighboring areas (within a radius of about 15 voxels). In particular, this allows us simulate "normal" asymmetries such as the brain torque.

Third, an additive, stationary, Gaussian white noise (standard deviation of 3) is added, on top of the "natural" noise of the original MR image. Fourth, after a proper coordinate system has been defined (see Figure 7), we successively apply a roll rotation of angle γ around the postero-anterior axis, a yaw rotation of angle β around the bottom-top axis, and a translation t along the left-right axis. If we consider the parameterization of the rotations by the Euler angles, this amounts to say that we apply the rigid transformation R_1, which consists in the rotation $R(0, \beta, \gamma)$ (pitch angle of 0, yaw angle of β, roll angle of γ), and the translation t along the left-right axis.

We choose the angles β and γ in the set {0, 3, 6,..., 21} (in degrees), and the translation t in the set {0, 4, 8,..., 20} (in voxels): the 384 possible combinations constitute the dataset A; note that, in order not to bias the overall results, the applied noise is different in each image. By resampling I_1 to the size 64^3, we get the image I_2. Adding the same lesions, expansions and shrinkings, random noise,

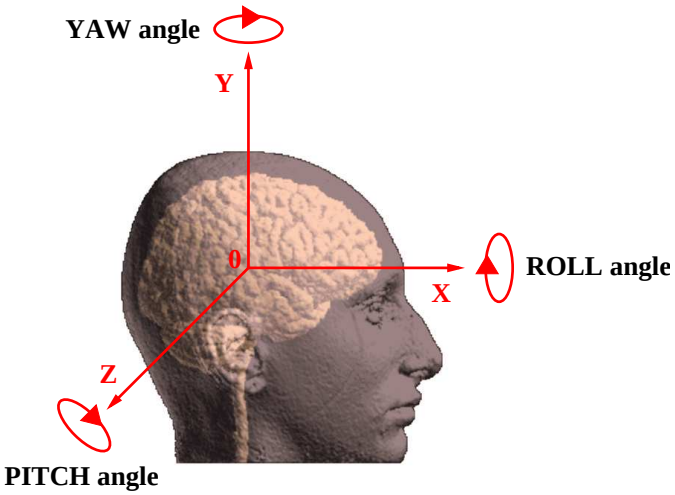

Fig. 7. **Coordinate system of I_1 and I_2.** In the grid of the perfectly symmetrical images I_1 and I_2, we define the axis x (resp. y, z) along the postero-anterior (resp. bottom-top, left-right) directions with respect to the head. In this coordinate system, the symmetry plane is displayed at position $z = 0$. Any vectorial rotation can be parameterized by the three Euler angles (named roll, yaw and pitch) around these axes.

rotations, and translations of 0, 2,..., 10 voxels in I_2, we get a second dataset of 384 images (dataset B). At last, a strong multiplicative bias field (linear in x, y and z) is added to I_2 before applying the rigid transformation, which creates a third dataset of 384 images (dataset C). This bias field creates large intensity variations within the same tissue across the image (for instance, the intensity of the white matter voxels ranges from 100 to 180, depending on their location in the 3D volume). In brief, we get the 3 following datasets:

- dataset A: I_1 + lesions + deformations + noise + 2 rotations + 1 translation
- dataset B: I_2 + lesions + deformations + noise + 2 rotations + 1 translation
- dataset C: I_2 + lesions + deformations + noise + bias + 2 rotations + 1 translation

B. Methods

For these 3 datasets, we run the program as follows:

- Experiment 1: dataset A with $(N, \Omega, \Delta, \Sigma) = (32, 32, 8, 8)$
- Experiment 2: dataset A with $(N, \Omega, \Delta, \Sigma) = (16, 16, 4, 4)$
- Experiment 3: dataset B with $(N, \Omega, \Delta, \Sigma) = (16, 16, 4, 4)$
- Experiment 4: dataset C with $(N, \Omega, \Delta, \Sigma) = (16, 16, 4, 4)$

For each of these experiments, we propose two measures of error to evaluate the accuracy of the algorithm. Given the applied rigid transformation R_1, we compute R_2 which realigns the estimated mid-sagittal plane with the center of the image grid. This means that the estimation is perfect if $R_2 \circ R_1$ leaves P invariant. $R_2 \circ R_1$ is not necessarily the identity; if $R_2 \circ R_1$ is a rotation around the left-right axis, or

a translation in the sagittal plane, P is invariant. It can be demonstrated that P (whose equation is $z = 0$) is invariant with respect to a rigid transformation if and only if the roll and yaw angles of its rotation, and the left-right component of its translation are equal to 0. In fact, this is stricly true if we know that the three Euler angles are lower than 90 degrees, which can be supposed in our case where $R_2 \circ R_1$ is likely to be close to the identity. The closer to zero these three parameters (two rotations and one translation), the more accurate the result; they constitute our first measure of error.

Another (and more concise) measure ε is described in Figure 8. It is computed on a bounding box of the head (in fact, the limits of the image grid), and thus gives a majorant of the error that is made in the overall brain volume. Following the same idea, we propose an analogous measure to evaluate the initial tilt of the head (*i.e.*, after the transformation R_1 has been applied). This measure δ (see Figure 8) is more concise than the three parameters characterizing R_1, but is non-univocal: different combinations of roll, yaw angles and translation along the left-right axis can yield the same δ. We will show that the algorithm has a breakdown point below which all the experiments can be considered as successful (see Figure 11). The value δ_{max} characterizing this breakdown point gives an idea of the robustness of the algorithm.

Comparing the experiments 1 and 2 (resp. 1 and 3) shows the influence of the initial size of the blocks (resp. subsampling) on the accuracy, the robustness and the computation time of the algorithm. Comparing the experiments 3 and 4 shows the sensitivity of the algorithm to bias effects. The experiments were run on a standard PC (OS Linux), 450 MHz, 256 MBytes of RAM.

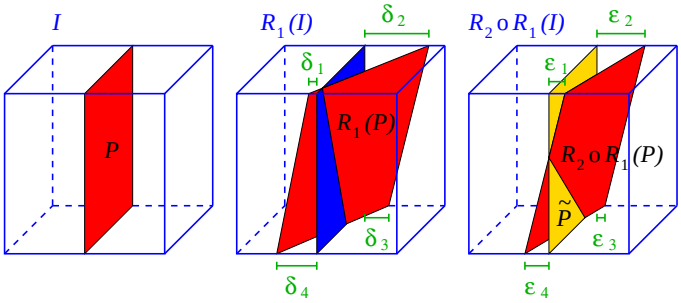

Fig. 8. **A measure of accuracy.** A synthetic image I (I_1 in the text) is generated, in which the plane P is the sought mid-sagittal plane of the brain (left sketch). We apply roll, yaw angles, and a translation along the left-right axis, which yields a rigid transformation R_1. In $R_1(I)$, the real mid-sagittal plane $R_1(P)$ is no longer aligned with the center of the grid (central sketch). The maximum δ of the four distances $\delta_1, \delta_2, \delta_3, \delta_4$, measures the tilt of the head before we run the algorithm. We estimate a mid-sagittal plane $\tilde{P}$ and a rigid transformation R_2 so that $\tilde{P}$ is displayed in the center of $R_2 \circ R_1(I)$ (right sketch). The estimated plane $\tilde{P}$ is generally different from the real one $R_2 \circ R_1(P)$. A measure of error is the maximum ε of the four distances $\varepsilon_1, \varepsilon_2, \varepsilon_3, \varepsilon_4$, that is $d(\tilde{P}, R_2 \circ R_1(P))$. This measure gives an idea of the maximum error made in the whole volume of the image, and is analogous to the measure used in the case of rigid registration [40], and based on the errors made at the 8 corners of a bounding box of the head.

C. Results and interpretation

Experiment 1 vs 2. The algorithm proved to be highly robust for the experiment 1. It never failed when δ was lower than 51 voxels, which corresponds (for example) to parameters (yaw,roll,translation)=$(15, 15, 16)$, $(18, 18, 8)$ or $(21, 21, 0)$. In real images, the tilt of the head is usually far smaller. For the experiment 2, the rate of success is reduced: the algorithm systematically succeeded when δ was lower than 42, which approximately corresponds to parameters $(12, 12, 16)$, $(15, 15, 18)$ or $(18, 18, 0)$. The smaller initial block size and the restricted neighborhood of search explain that the algorithm is less able to deal with too tilted heads. Compared to experiment 1, there is one less scale to explore, and the average computation time is reduced, but still prohibitive (about 34 min). The obtained accuracy is about the same compared to experiment 1. As a conclusion, the set of initial parameters $N = ([X/4], [Y/4], [Z/4])$ seems to be best adapted at a given resolution of the image.

Experiment 1 vs 3. For these two datasets, studied with optimal initial block size (respectively, $N = (32, 32, 32)$ and $N = (16, 16, 16)$), the robustness is about the same. The subsampling does not reduce significantly the efficiency of the algorithm, which never failed when δ was lower than 25 voxels; for example, this corresponds to parameters $(15, 15, 8)$, $(18, 18, 4)$ or $(21, 21, 0)$, comparable with the parameters of experiment 1. The accuracy is divided by two in experiment 3 compared to experiments 1 and 2, but remains very high (see Table II). At last, the computation time is strongly reduced (by a factor of 10). This suggests that highly subsampled images (from 256^3 to 64^3) are enough for a satisfying estimation of the mid-sagittal plane.

Experiment 3 vs 4. The algorithm is very robust with respect to a relatively high level of bias field, which does not degrade the accuracy of the algorithm. To our mind, this is an important feature of this local approach. Locally, the intensity variations are smaller than on the whole image, and the CC seems to remain a sensible similarity measure.

Conclusion. A sample output of the algorithm is displayed in Figure 9. The results of the experiment 2 are displayed in Figure 11, and illustrate the typical behavior of the algorithm. There is a clear breakdown point below which all the experiments can be considered as successful, as they exhibit a very high accuracy (see Table II). Beyond this breakdown point, with the same tilt, some experiments have failed, and some others have successed. This is explained by the fact that the measure of the tilt δ is non-univocal: a transformation R_1 with large roll and yaw angles, and small translation along the left-right axis can yield the same tilt as another transformation with small angles and large translation. Practically, we observed that the performances of the algorithm are better on the latter. Our interpretation is that the algorithm finds it easier to deal with large translations than large rotations because of the parallelepipedic rectangular shape of the blocks. In

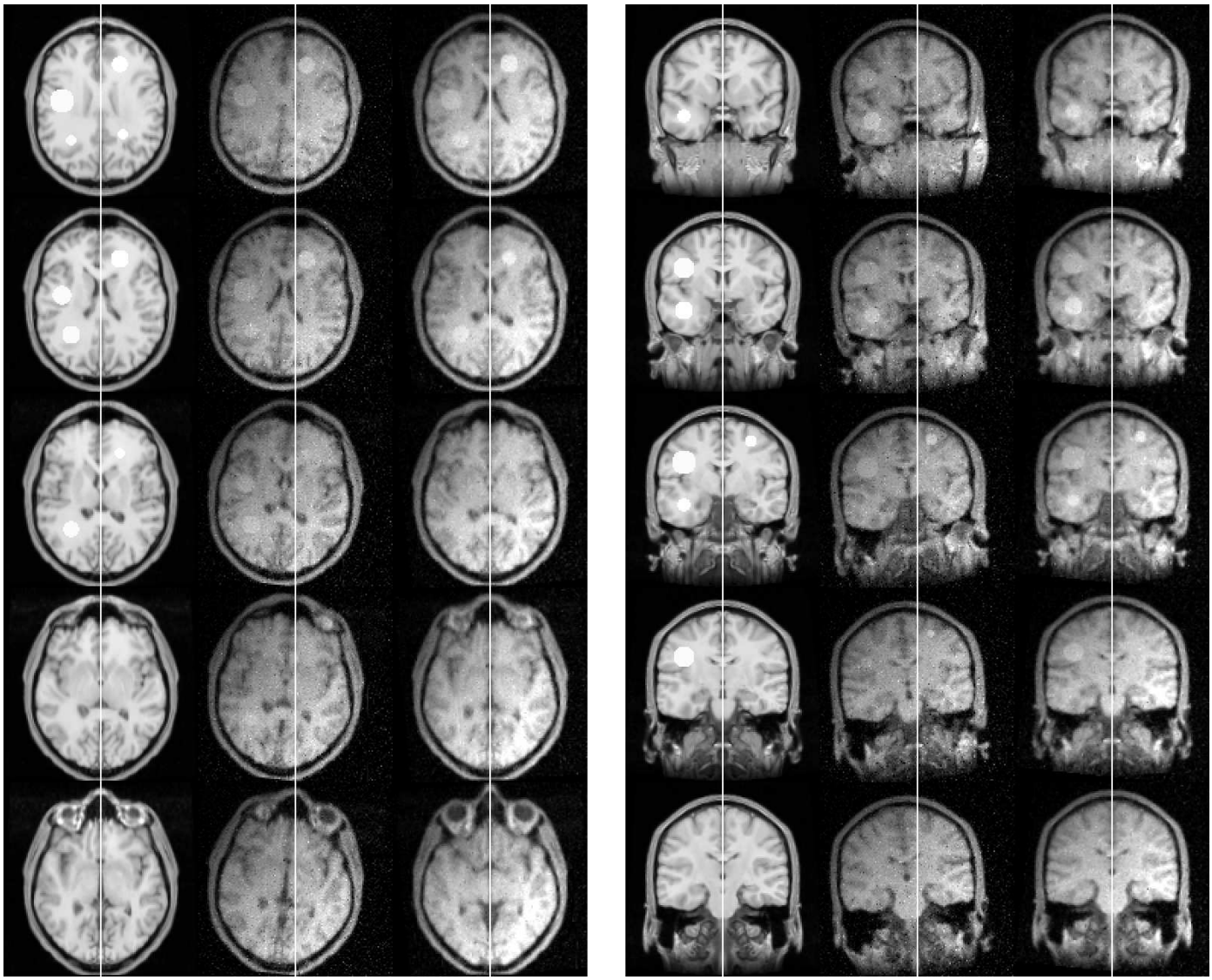

Fig. 9. **Realignment of a synthetic MR image.** Artificial lesions, expansions and shrinkings, random noise and bias field are added to a perfectly symmetrical MR image of size 128^3. Roll and yaw angles of 6 degrees, and a translation along the left-right axis of 6 voxels are applied to this image. The initial parameters of the block matching algorithm are $(N, \Omega, \Delta, \Sigma) = (16, 16, 4, 4)$. The roll, yaw angles, and translation along the left-right axis of $R_2 \circ R_1$ are 0.04, 0.03 degrees and 0.1 voxels. The error ε is 0.2 voxels (see Figure 8). We display 2 panels with axial (left) and coronal (right) views. In each panel, from left to right, we display the original image with added lesions, expansions and shrinkings, the tilted image with added noise and bias field, and the realigned image.

Figure 10, we display the output of the block matching procedure when the algorithm has converged, which illustrates its behavior with respect to normal and abnormal asymmetries.

In brief, we draw the following conclusions from the four experiments. There is a clear breakdown point, below which the algorithm always succeeds with very high accuracy. This point measures the robustness of the algorithm. For a usual MR image with 256^3 voxels of size 0.78mm^3, this breakdown point correspond to a tilt δ of about 100 voxels (50 for the subsampled image of size 128^3, 25 for the subsampled image of size 64^3). When we apply the algorithm on the subsampled image of size 64^3, using $(16, 16, 4, 4)$ as initial parameters, we reach a precision of about $\varepsilon = 10.10^{-2} \times 4 \times 0.78 \simeq 0.3$ mm (see Table II) below the breakdown point (error computed according to Figure 8) within a CPU time of about 3 minutes. For more strongly tilted images, which to our knowledge are very rarely met in real acquisitions (Section IV), an initial alignment along the principal axes of inertia of the head can be a useful preprocessing step.

IV. Validation and results on real images

A. Validation

It is difficult to carry out a proper validation on real medical images, for which no ground truth exists about the "true" mid-sagittal plane. We give a mathematical definition of this plane, as the one making the two parts of the head lying on each side most similar. As a consequence, a comparison between a manually outlined plane

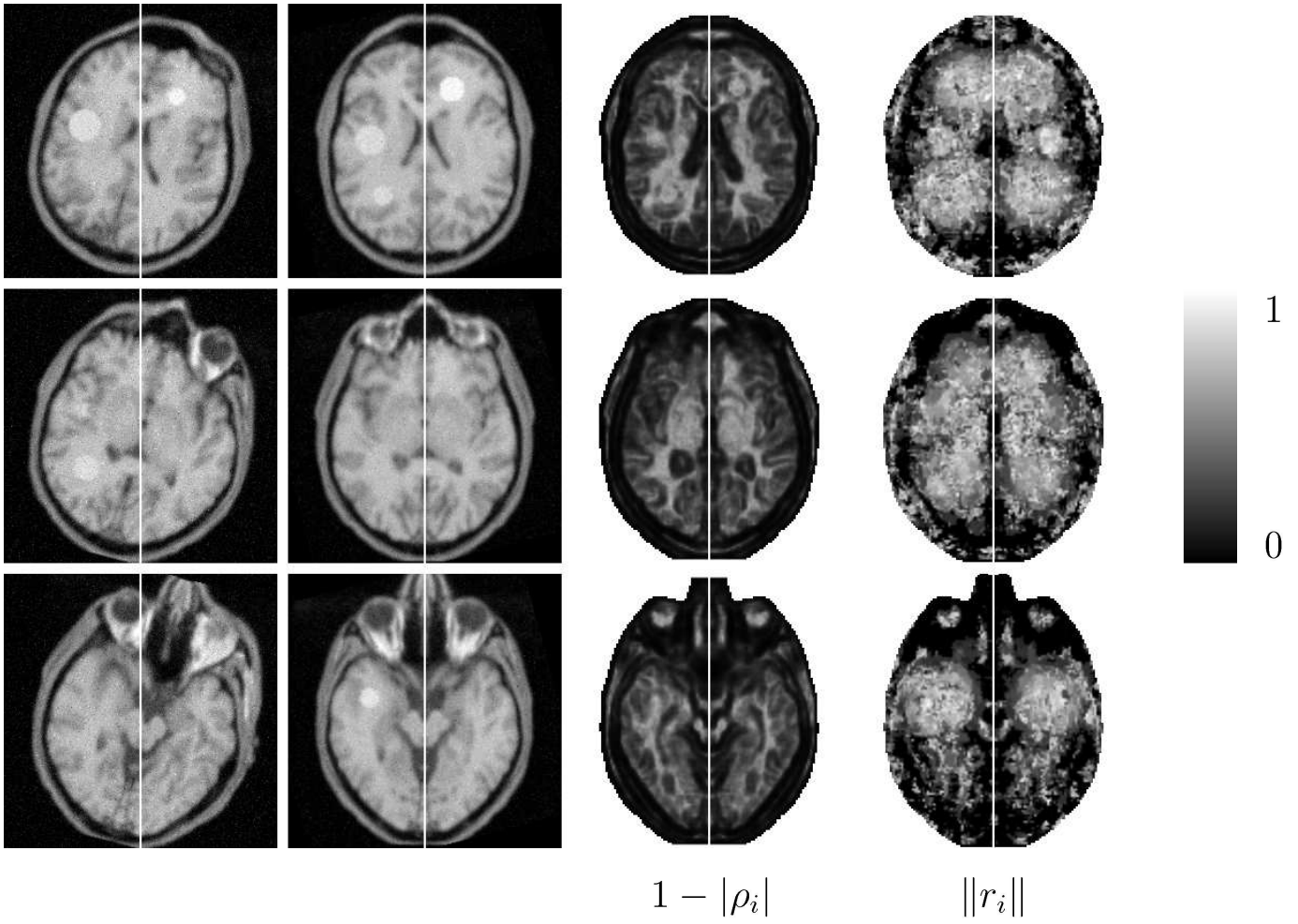

Fig. 10. **Local correlations and displacements.** Left panels: initial synthetic image and its realigned version. When the mid-sagittal plane P has been identified, we perform a block matching between the realigned image and its reflection with respect to P, with parameters $(N, \Omega, \Delta, \Sigma) = (4, 4, 1, 1)$. For each voxel i, the information provided by the block matching procedure is twofold: first, the CC between the matched blocks (ρ_i), and second, the displacement vector that connects them (r_i). We display the values of the absolute correlation coefficients $\{|\rho_i|\}$, or rather, $\{1 - |\rho_i|\}$, which underline the areas in weak correlation (high gray level values). The latter grossly correspond to the places where synthetic lesions, expansions or shrinkings have been applied; a threshold on the absolute CC allows to eliminate a part of these asymmetries, as well as the majority of the background voxels. We also display the normalized norms $\{|r_i|/|r_{max}|\}$ of the displacements (*i.e.*, the normalized residuals). The areas with high gray level values exhibit residuals with a large norm, and are naturally eliminated during the robust LTS estimation. They correspond to areas where severe synthetic asymmetries have been added. An analogous illustration is shown in Figure 15 for a real MR image.

based on the interhemispheric fissure and our "symmetry" plane is not necessarily informative. In a nutshell, a plane perfectly fitting the longitudinal fissure is not necessarily the best "symmetry" plane, which takes into account the whole brain volume. The quantitative evaluation of such a plane is consequently difficult; in our case, a visual evaluation has been carried out by clinicians. In practice, the algorithm has been successfully applied on a high number of MR images, as well as on a few images of other modalities (CT, PET, SPECT), as shown in the next subsection.

However, in this subsection we propose a small validation on real images, based on two experiments on PD- and T2-weighted MR images of a patient with multiple sclerosis, acquired at the same time. We thus expect the computed mid-sagittal plane to be the same for both images. These two images have been provided by the State University of New York at Stony Brook, USA, within the EC funded BIOMORPH project (Development and Validation of Techniques for Brain Morphometry, 1996-1999, web address: http://www.ia.unc.edu/public/styner/biomorph). They contain $256 \times 256 \times 52$ voxels of size $0.9 \times 0.9 \times 2.5$ mm^3.

In a first experiment, we computed the roll, yaw angles and translation along the left-right axis of the composed transformation $R_{PD} \circ R_{T2}^{-1}$, where R_{PD} and R_{T2} are rigid transformations that realign the estimated mid-sagittal plane in both cases. These values are respectively equal to 0.17, 0.03 degrees, and -0.45 voxels, which shows very good accordance between the two estimated planes (Figure 12).

In a second experiment, we added severe artefacts on both the PD-weighted and the T2-weighted image (Fig-

Exp.	Robustn. (δ_{max})	Accuracy (RMS errors)				CPU Time
		Roll	Yaw	Transl.	ε	
1	51	0.04	0.04	0.05	0.11	$45'$
2	42	0.03	0.04	0.05	0.10	$34'$
3	25	0.11	0.09	0.06	0.13	$3'$
4	25	0.11	0.08	0.07	0.11	$3'$

TABLE II

Results. The RMS errors (indicated for tilts below the breakdown point) are measured in degrees for the roll and yaw angles and voxels for the left-right translation and ε (see Figure 8). The RMS errors are computed on the whole set of images for which $\delta < \delta_{max}$, *i.e.*, below the breakdown point (see also Figure 11). The errors are doubled between experiments on 128^3 and 64^3 images, including for the translation and ε (the errors in voxels are about the same, and the errors in mm are doubled for half resolution images).

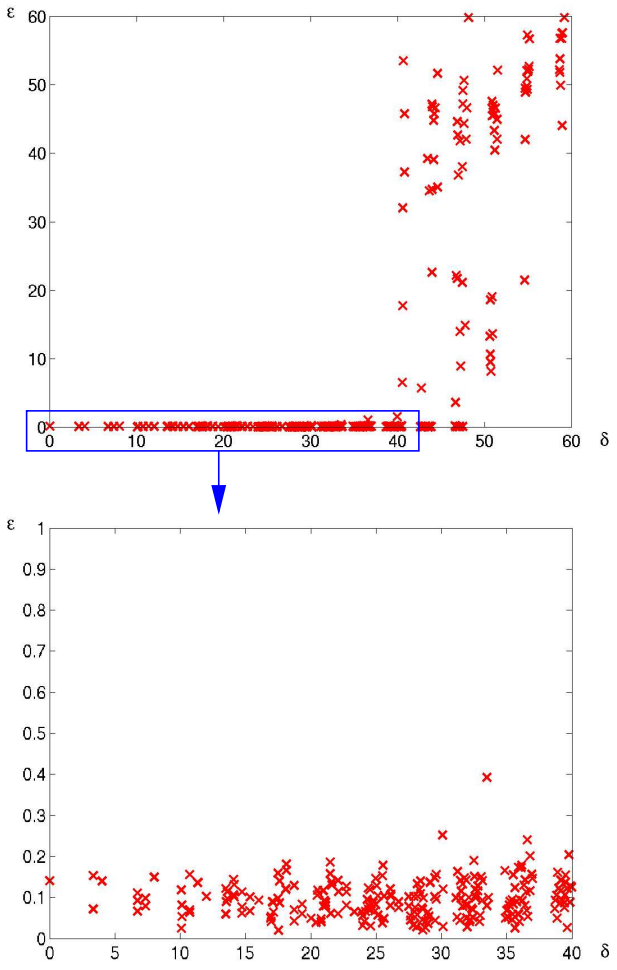

Fig. 11. **The breakdown point of the algorithm.** As an indication, we display the results of experiment 2. The units of δ and ε are voxels. A clear breakdown point appears (top): for every image with $\delta_{max} < 42$ voxels, the accuracy of the algorithm is excellent ($\varepsilon < 0.2$ voxels), as displayed on the enlarged graph (bottom).

ure 13); these artefacts cover a fifth of the total head volume. We computed the rigid transformations R^*_{PD} and R^*_{T2} which realign the mid-sagittal planes estimated on these strongly corrupted images. The roll, yaw angles and translation along the left-right axis of the composed transformation $R^*_{PD} \circ R^{-1}_{PD}$ (resp. $R^*_{T2} \circ R^{-1}_{T2}$) are equal to -0.20, -0.02 degrees and 0.35 voxels (resp. 0.10, -0.03 degrees and -0.13 voxels). This proves that the artefacts have not significantly affected the estimation of the mid-sagittal plane.

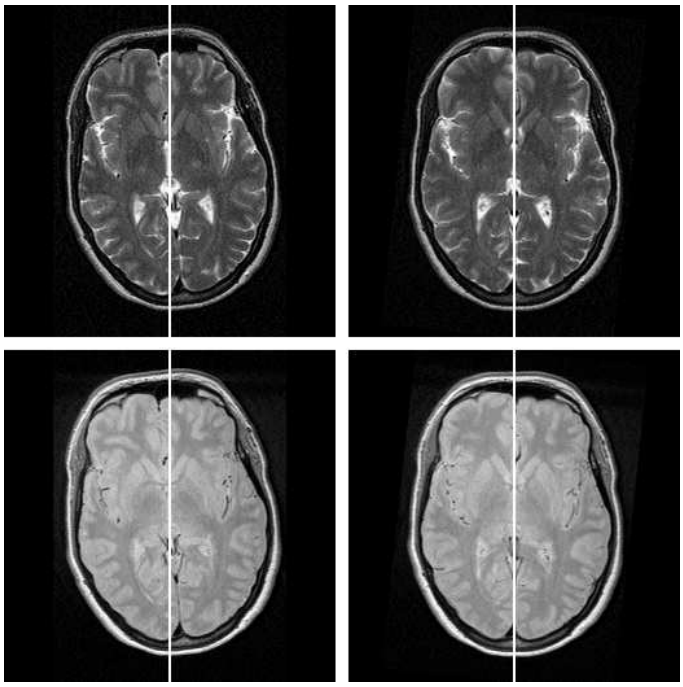

Fig. 12. **Anisotropic PD- and T2-weighted MR images.** Axial slices of the initial and the realigned and recentered PD- (top) and T2-weighted (bottom) images. The estimated planes are very similar ($R_{PD} \circ R^{-1}_{T2}$ has roll and yaw angles of 0.17 and 0.03 degrees, and a left-right translation component of about -0.45 voxels).

B. Results

The algorithm has been applied on more than 250 MR images (Section IV-B.1), as well as on a few images of other modalities such as CT, PET, or SPECT (Section IV-B.2). As previously explained, a proper validation on real images is difficult. The good quality of the results has been visually assessed by clinicians. In the following, we provide a series of significative results on isotropic and anisotropic, normal and pathological, anatomical and functional images.

B.1 MR images

The algorithm has been extensively used on MR images within three different projects. As a whole, more than 250 MR images were processed. First, in collaboration with the MARIARC (Magnetic Resonance and Image Analysis Research Centre), University of Liverpool, UK, we compared the brain structural asymmetry between normal males and females [41], [42]. Second, within the previously quoted BIOMORPH project,

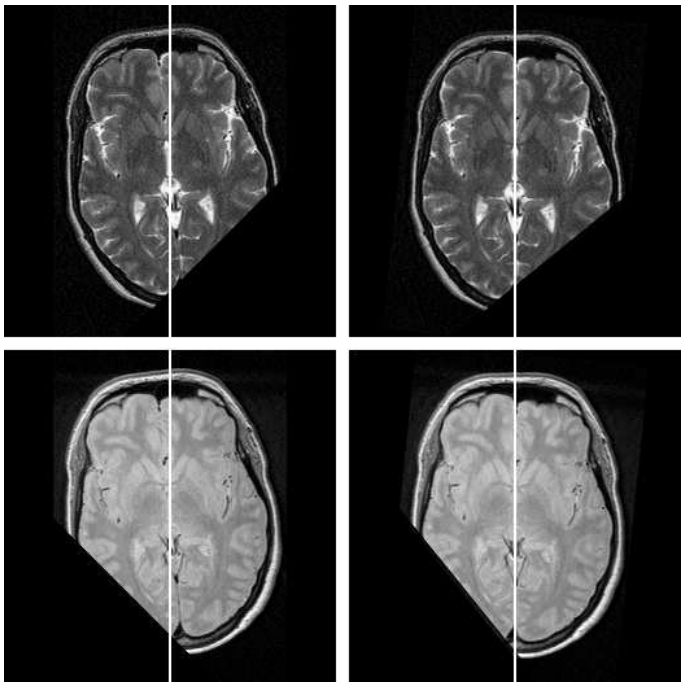

Fig. 13. **Anisotropic PD- and T2-weighted MR images with artefacts added.** Same layout as Figure 12. When artificial severe artefacts are added (they are different in both cases), the estimation of the planes is not significantly affected. In both cases, these artefacts cover the fifth of the total head volume. If we note R^*_{PD} (resp. R^*_{T2}) the computed rigid transformation that realigns the estimated mid-sagittal plane of the PD-(resp. T2-)weighted MR image with the artefact added, the roll, yaw angles, and the left-right translation component of $R^*_{PD} \circ R^{-1}_{PD}$ (resp. $R^*_{T2} \circ R^{-1}_{T2}$) are equal to -0.20, -0.02 degrees and 0.35 voxels (resp. 0.10, -0.03 degrees and -0.13 voxels).

we performed the same comparison between normal controls and schizophrenics patients [14]. Third, within the EC funded QAMRIC project (Quantitative Analysis of MR Scans in Creutzfeldt-Jakob Disease, 1998-2001, web address: http://www-sop.inria.fr/epidaure/QAMRIC), we are currently studying the symmetry of hypo- or hypersignals in brain structures such as the pulvinar [43].

In this subsection, we present four sets of results obtained on normal as well as pathological subjects, notably taken from these different projects we have been involved in.

- MR, T1-weighted (256^3 voxels of size 0.78mm^3). Provided by Dr. Neil Roberts, MARIARC, University of Liverpool, UK. Displayed in Figure 14. For this normal subject, we also show the maps of correlations and normalized residuals as in Figure 10. Displayed in Figure 15.
- MR, T1-weighted ($256 \times 256 \times 52$ voxels of size $0.9 \times 0.9 \times 2.5$ mm^3). Provided by the State University of New York at Stony Brook, USA, within the BIOMORPH project. We display two panels of 10 subjects each. The first panel is made of normal controls (Figure 16). The second panel is made of schizophrenic patients (Figure 17).
- MR, T1-weighted ($256 \times 256 \times 19$ voxels of size $0.9 \times 0.9 \times 6.5$ mm^3). Provided by the QAMRIC project. Patient with sporadic Creutzfeldt-Jakob disease. Displayed in Figure 18.
- MR, T1-weighted ($256 \times 256 \times 24$ voxels of size $0.9375 \times 0.9375 \times 6$ mm^3). Provided by Dr. Pierre-Yves Bondiau, Centre Antoine Lacassagne, Nice, France. Patient with brain cancer. Displayed in Figure 19.

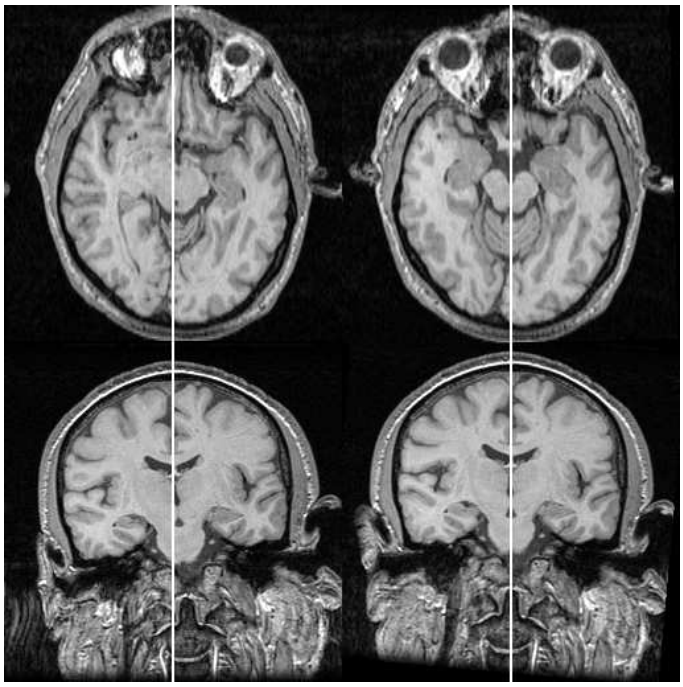

Fig. 14. **Isotropic T1-weighted MR image.** Axial (top) and coronal (bottom) views of the initial 3D image (left) and the reoriented and recentered version (right). Normal subject. Maps of correlations and normalized residuals are provided for this subject in Figure 15.

B.2 CT, PET, and SPECT images

In this subsection, we present a few results on other anatomical (CT) and functional (SPECT, PET) modalities. Note that, as implemented, our algorithm cannot deal with images with varied slice thickness, sometimes found in some CT images.

- CT ($256 \times 256 \times 203$ voxels of size 0.6 mm^3). Provided by the Radiology Research Imaging Lab, Mallinckrodt Institute of Radiology, Saint Louis, Missouri, USA. Displayed in Figure 20.
- PET ($128 \times 128 \times 15$ voxels of size $2.05 \times 2.05 \times 6.75$ mm^3. Provided by the Hammersmith Hospital, London, UK, and the Unité 230 of INSERM, Toulouse, France. Displayed in Figure 21.
- SPECT (64^3 voxels of size 4 mm^3). Provided by Pr. Michael L. Goris, Department of Nuclear Medicine, Stanford University Hospital, California, USA. Displayed in Figure 22.

V. Conclusion

We have presented a new symmetry-based method allowing to compute, reorient and recenter the mid-sagittal plane in volumetric anatomical and functional images of the head. Our iterative approach relies on the matching of homologous anatomical structures or functional areas on both sides of the brain, and a robust estimation of the

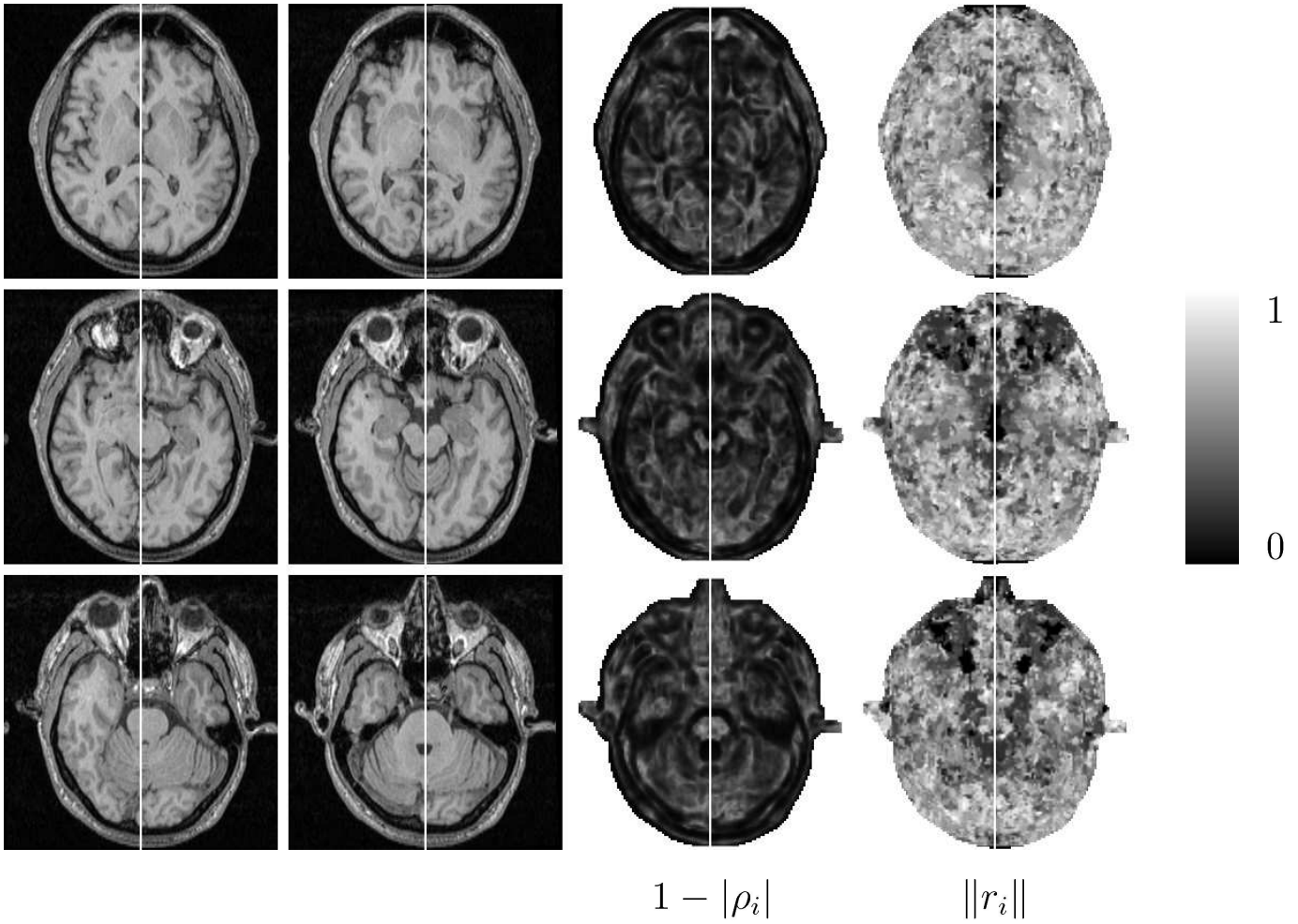

Fig. 15. **Isotropic T1-weighted MR image.** Same layout as Figure 10, for the subject of Figure 14. In particular, it shows that the occipital lobes are in weak correlation, which confirms their visible asymmetry. Moreover, the displacement vectors associated with both the occipital and the frontal lobes have a large norm, which confirms the torque effect. The areas with large absolute correlation and residuals with large norms are taken into account for the estimation of the plane. We notice that, in this image, head structures such as the eyes and interhemispheric cerebral areas are particularly symmetrical.

plane best superposing these pairs of counterparts. The algorithm is iterative, multiscale, fully automated, and provides a useful tool for further symmetry-based analysis of the brain; it has already been successfully applied on a database of more than one hundred subjects. We showed on a large database of synthetic images that we could obtain a subvoxel accuracy in a CPU time of about 3 minutes, for strongly tilted heads, even in presence of strong acquisition noise and bias field. We have presented results on isotropic and anisotropic, normal and pathological images on several anatomical and functional modalities (MR, CT, SPECT and PET).

Acknowledgments

The authors would like to thank Jean-Philippe Thirion, Gérard Subsol, Neil Roberts and Tom Barrick for fruitful discussions about this work. We would also like to thank D.L. Collins for proofreading of this article.

Appendix 1: LS estimation of the mid-sagittal plane

We want to minimize:

$$C = \sum_i (a_i - S_P(a_i''))^2 \tag{1}$$

with $S_P(a_i'') = a_i'' - 2((a_i'' - p)^\top n)n$ and where p is a point in the symmetry plane and n the unit normal vector to the plane. By differentiating C with respect to p, we get:

$$\left(\frac{dC}{dp}\right)^\top = 4\sum_i (2p - a_i'' - a_i)^\top nn^\top \tag{2}$$

which demonstrates that the barycenter G:

$$G = \frac{1}{n}\sum_i \frac{(a_i'' + a_i)}{2} \tag{3}$$

belongs to the symmetry plane. Substituting G in equation 1 and simplifying the equation, we get:

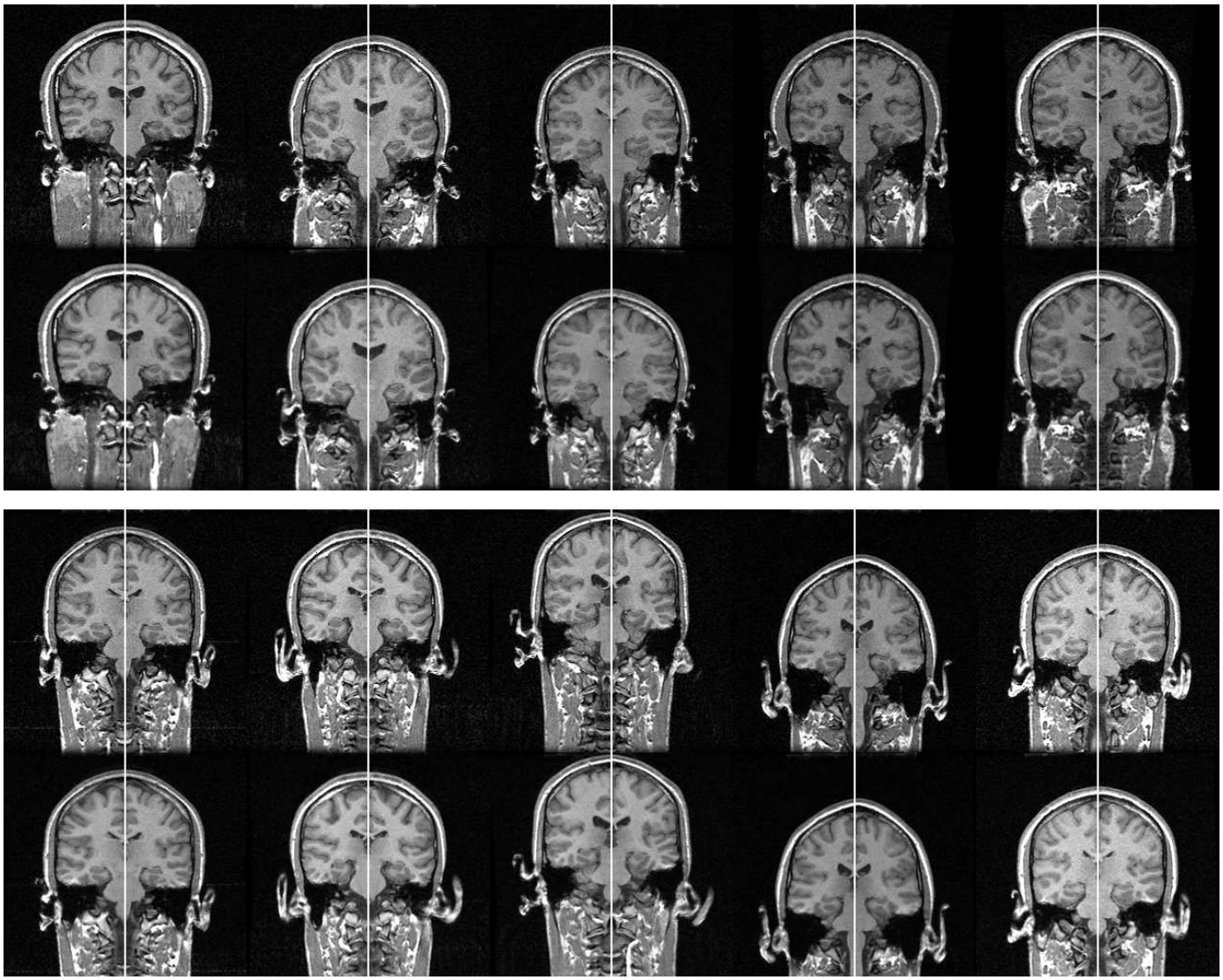

Fig. 16. **Panel of T1-weighted MR images (normal controls).** Axial views of the initial 3D image (top) and the reoriented and recentered version (bottom). The initial tilt of the head is small for most of these subjects, as in Figure 17.

$$C = \sum_i (a_i'' - a_i)^2 + 4[(a_i'' - G)^\top n][(a_i - G)^\top n] \quad (4)$$

which is minimized when the following expression is minimized:

$$\sum_i n^\top [(a_i - G)(a_i'' - G)^\top] n \quad (5)$$

which means than n is the eigenvector associated to the smallest eigenvalue of I, where:

$$I = \sum_i (a_i - G)(a_i'' - G)^\top \quad (6)$$

Appendix 2: Realignment of the mid-sagittal plane

We want to demonstrate that $R^{1/2}(I)$ is an image where the mid-sagittal plane P is displayed in the center of the image grid ($R = S_K \circ S_P$). This is equivalent to demonstrating that the images $R^{1/2}(I)$ and $R^{1/2}(S_P(I))$ are symmetrical with respect to K, that is:

$$S_K \circ R^{1/2}(I) = R^{1/2} \circ S_P(I) \quad (7)$$

To demonstrate this, note that S_P is a planar symmetry, and therefore $S_P \circ S_P = Id$. This allows to write:

$$R = S_K \circ S_P \Rightarrow S_K = R \circ S_P \quad (8)$$

Furthermore, as $R^{1/2}$ is an affine rotation with a rotation axis in $P \cap K$ (provided P and K are not parallel), $S_K \circ R^{1/2}$ is also a planar symmetry, hence:

$$S_K \circ R^{1/2} = (S_K \circ R^{1/2})^{-1} = R^{-1/2} \circ S_K^{-1} = R^{-1/2} \circ S_K \quad (9)$$

Replacing S_K with $R \circ S_P$ in equation 9 (on the right) gives the desired relation:

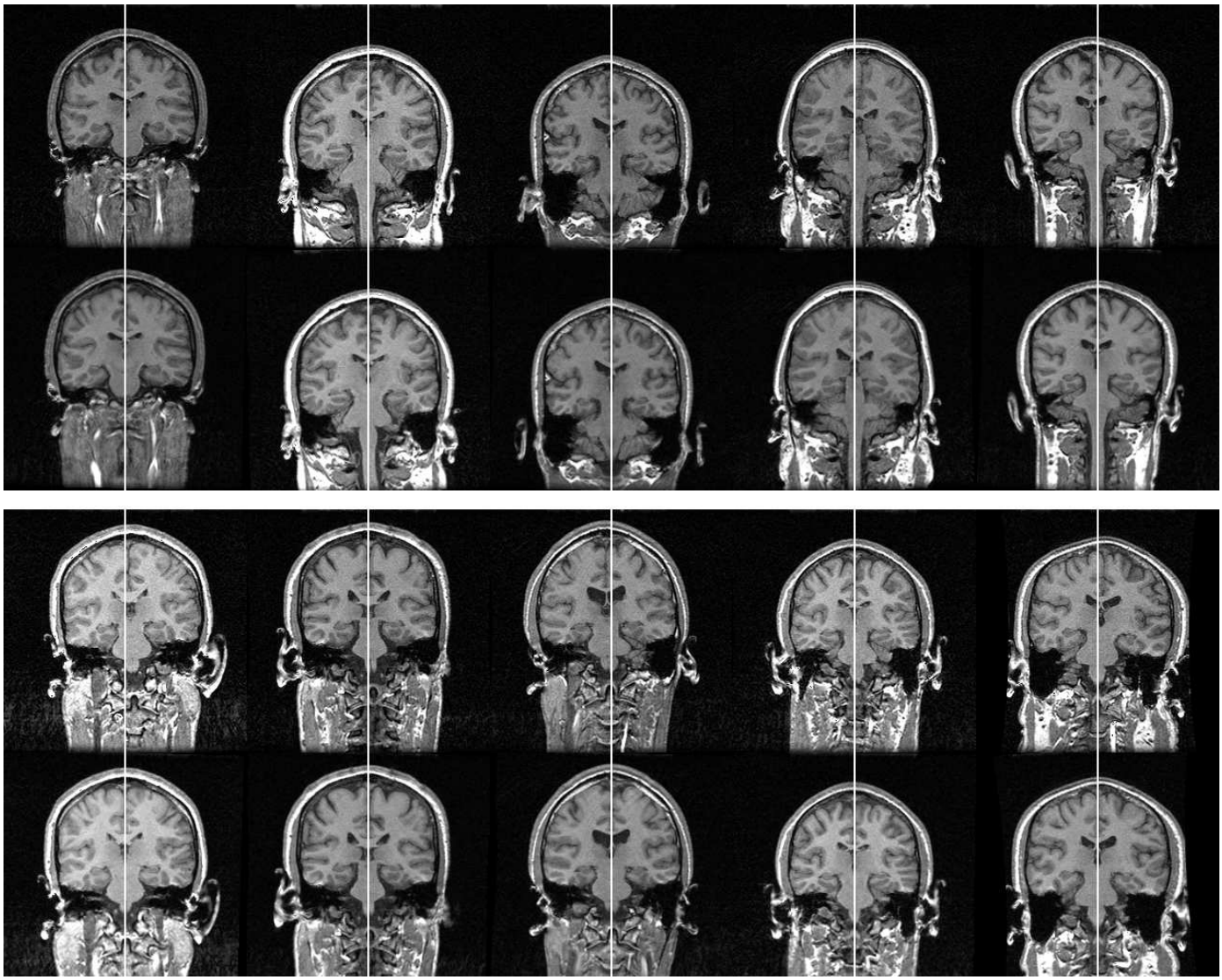

Fig. 17. **Panel of T1-weighted MR images (schizophrenic patients).** Same layout as Figure 16.

$$S_K \circ R^{1/2} = R^{-1/2} \circ R \circ S_P = R^{1/2} \circ S_P \qquad (10)$$

The same relation can be easily demonstrated if P and K are parallel.

References

[1] J.F. Iaccino, *Left Brain-Right Brain Differences: Inquiries, Evidence and New Approaches*, Lawrence Erlbaum Associates, Hillsdale, New Jersey, 1993.

[2] N. Geschwind and W. Levitsky, "Left-right asymmetry in temporal speech region," *Science*, vol. 161, pp. 186–187, 1968.

[3] H. Steinmetz, J. Volkmann, L Jancke, and H.J. Freund, "Anatomical left-right asymmetry of language-related temporal cortex is different in left- and right-handers," *Annals of Neurology*, vol. 29, no. 3, pp. 315–319, 1991.

[4] A. Kertesz, M. Polk, Black S.E., and J. Howell, "Sex, Handedness and the Morphometry of Cerebral Asymmetries on MRI," *Brain Research*, vol. 530, pp. 40–48, 1990.

[5] T.H. Williams, N. Gluhbegovic, and J.Y. Jew, "Virtual Hospital," 1997, University of Iowa. WEB access: http://www.vh.org/Providers/Textbooks/BrainAnatomy/-BrainAnatomy.html.

[6] M. Zeidler, R.J. Sellar, D.A. Collie, R. Knight, G. Stewart, M.A. Macleod, J.W. Ironside, S. Cousens, A.C. Colchester, D.M. Hadley, and R.G. Will, "The pulvinar sign on magnetic resonance imaging in variant Creutzfeldt-Jakob disease," *Lancet*, vol. 355, pp. 1412–1418, 2000.

[7] C. Oppenheim, J.-P. Brandel, J.-J Hauw, J.-P. Deslys, and B. Fontaine, "MRI and the second French case of nvCJD," *Lancet*, vol. 356, pp. 253, 2000.

[8] S. Minoshima, K.A. Frey, R.A. Koeppe, N.L. Foster, and D.E. Kuhl, "A diagnostic approach in Alzheimer's disease using three-dimensional stereotactic surface projections of fluorine-18-FDG PET," *Journal of Nuclear Medicine*, vol. 36, no. 7, pp. 1238–48, 1995.

[9] A.M. Galaburda, J. Corsiglia, G.D. Rosen, and G.F. Sherman, "Planum temporale asymmetry, reappraisal since Geschwind and Levitsky," *Neuropsychologia*, vol. 25, no. 6, pp. 853–868, 1987.

[10] J.S. Kwon, R.W. McCarley, Y. Hirayasu, J.E. Anderson, I. Fisher, R. Kikinis, F.A. Jolesz, and M.E. Shenton, "Left Planum Temporale Volume Reduction in Schizophrenia," *Archives of General Psychiatry*, vol. 56, no. 2, pp. 142–148, 1999.

[11] T.J. Crow, "Schizophrenia as an anomaly of cerebral asymmetry," in *Imaging of the Brain in Psychiatry and Related Fields*, K. Maurer, Ed., pp. 1–17. Springer-Verlag, Berlin Heidelberg, 1993.

[12] R.M. Bilder, H. Wu, B. Bogerts, G. Degreef, M. Ashtari, J.M.J. Alvir, P.J. Snyder, and J.A. Lieberman, "Absence of regional hemispheric volume asymmetries in first-episode schizophrenia,"

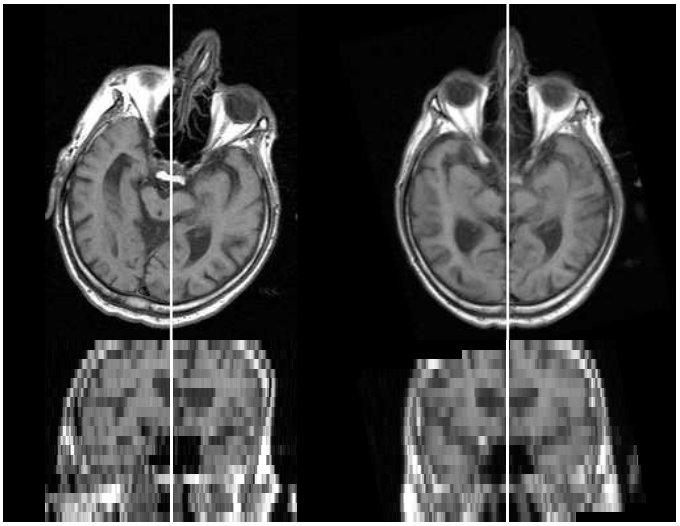

Fig. 18. **Anisotropic T1-weighted MR image.** Same layout as Figure 14. Patient with sporadic Creutzfeldt-Jakob disease. The three main difficulties raised by this image are: first, its low resolution, second, the large initial tilt of the head for both yaw and roll angles, making the symmetrical brain structure appear in different axial and coronal sections, and third, the occultation of the top of the brain.

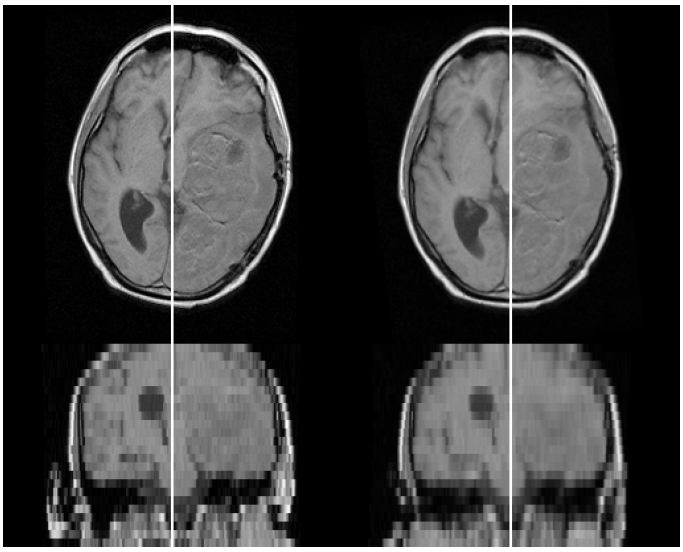

Fig. 19. **Anisotropic T1-weighted MR image.** Same layout as Figure 14. The three main difficulties raised by this image are: first, its low resolution, second, the presence of a brain tumor making the interhemispheric fissure and the ventricles severely displaced with respect to their normal positions, and third, the occultation of the top of the brain.

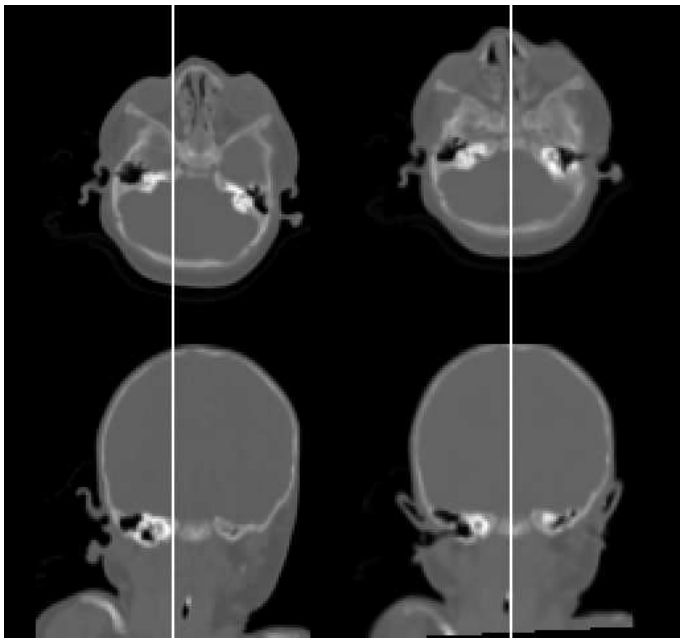

Fig. 20. **Isotropic CT image.** Same layout as Figure 14. As the brain does not appear clearly, the mid-sagittal plane is mainly computed from the bone structures.

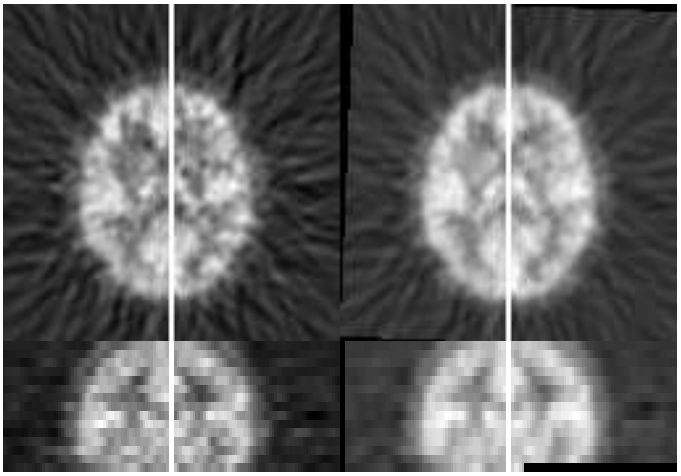

Fig. 21. **Anisotropic PET image.** Same layout as Figure 14.

American Journal of Psychiatry, vol. 151, no. 10, pp. 1437–1447, October 1994.

[13] P.C. Marais, R. Guillemaud, M. Sakuma, A. Zisserman, and M. Brady, "Visualising cerebral asymmetry," in *Visualization in Biomedical Computing VBC'96*, K.H. Höhne and R. Kikinis, Eds., Hamburg, Germany, September 1996, vol. 1131 of *Lecture Notes in Computer Science*, pp. 411–416, Springer.

[14] S. Prima, J.-P. Thirion, G. Subsol, and N. Roberts, "Automatic Analysis of Normal Brain Dissymmetry of Males and Females in MR Images," in *First International Conference on Medical Image Computing and Computer-Assisted Intervention, MICCAI'98*, W.M. Wells, A. Colchester, and S.L. Delp, Eds., Boston, USA, October 1998, vol. 1496 of *Lecture Notes in Computer Science*, pp. 770–779, Springer.

[15] J.-P. Thirion, S. Prima, G. Subsol, and N. Roberts, "Statistical Analysis of Normal and Abnormal Dissymmetry in Volumetric Medical Images," *Medical Image Analysis (MedIA)*, vol. 4, no. 2, pp. 111–121, June 2000, Electronic version: http://www.inria.fr/RRRT/RR-3178.html.

[16] M.E. Brummer, "Hough Transform Detection of the Longitudi-

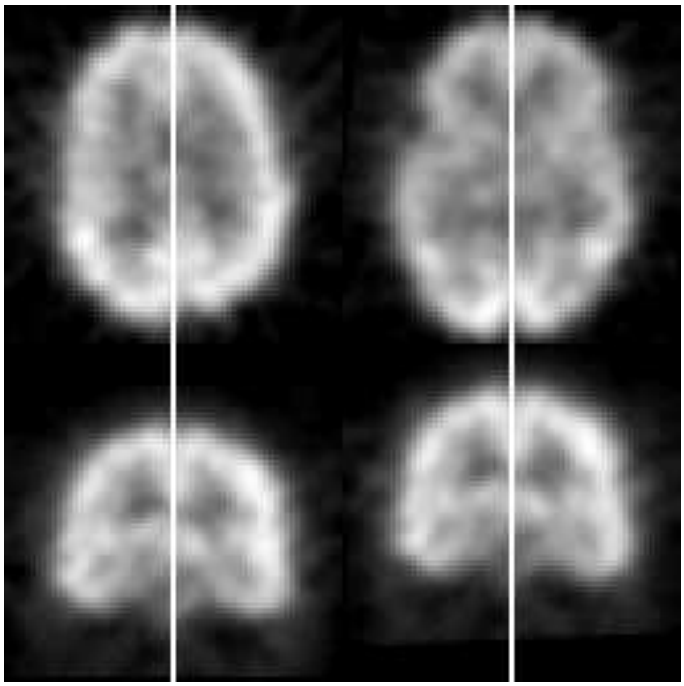

Fig. 22. **Isotropic SPECT image.** Same layout as Figure 14.

nal Fissure in Tomographic Head Images," *IEEE Transactions on Medical Imaging*, vol. 10, no. 1, pp. 74–81, March 1991.

[17] B.A. Ardenaki, J. Kershaw, M. Braun, and I. Kanno, "Automatic Detection of the Mid-Sagittal Plane in 3-D Brain Images," *IEEE Transactions on Medical Imaging*, vol. 16, no. 6, pp. 947–952, December 1997.

[18] S. Smith and M. Jenkinson, "Accurate Robust Symmetry Estimation," in *Second International Conference on Medical Image Computing and Computer-Assisted Intervention, MICCAI'99*, C. Taylor and A. Colchester, Eds., Cambridge, UK, September 1999, vol. 1679 of *Lecture Notes in Computer Science*, pp. 308–317, Springer.

[19] C. Sun and J. Sherrah, "3D Symmetry Detection Using The Extended Gaussian Image," *IEEE Transactions on Pattern Analysis and Machine Intelligence*, vol. 19, no. 2, pp. 164–168, 1997.

[20] Y. Liu, R.T. Collins, and W.E. Rothfus, "Automatic Bilateral Symmetry (Midsagittal) Plane Extraction from Pathological 3D Neuroradiological Images," in *SPIE, International Symposium on Medical Imaging*, San-Diego, USA, February 1998.

[21] Y. Liu, R.T. Collins, and W.E. Rothfus, "Robust midsagittal plane extraction from normal and pathological 3-D neuroradiology images," *IEEE Transactions on Medical Imaging*, vol. 20, no. 3, pp. 175–192, March 2001.

[22] L. Junck, J.G. Moen, G.D. Hutchins, M.B. Brown, and D.E. Kuhl, "Correlation Methods for the Centering, Rotation, and Alignment of Functional Brain Images," *Journal of Nuclear Medicine*, vol. 31, pp. 1220–1226, July 1990.

[23] S. Minoshima, K.L. Berger, K.S. Lee, and M.A. Mintun, "An Automated Method for Rotational Correction and Centering of Three-Dimensional Functional Brain Images," *Journal of Nuclear Medicine*, vol. 33, pp. 1579–1585, August 1992.

[24] C. Sun, "Symmetry detection using gradient information," *Pattern Recognition Letters*, vol. 16, pp. 987–996, 1995.

[25] A. Venot, J.-F. Lebruchec, and J.-C. Roucayrol, "A New Class of Similarity Measures for Robust Image Registration," *Computer Vision, Graphics, and Image Processing*, vol. 28, no. 2, pp. 176–184, 1984.

[26] P. Gerlot-Chiron and Y. Bizais, "Registration of Multimodality Medical Images Using a Region Overlap Criterion," *CVGIP: Graphical Models and Image Processing*, vol. 54, no. 5, pp. 396–406, September 1992.

[27] P.J. Rousseeuw and A.M. Leroy, *Robust Regression and Outlier Detection*, Wiley Series in Probability and Mathematical Statistics, 1987.

[28] J.-P. Thirion, "Image matching as a diffusion process: an analogy with Maxwell's demons," *Medical Image Analysis (MedIA)*, vol. 2, no. 3, pp. 243–260, September 1998.

[29] A.K. Jain, "Image data compression: a review," *Proceedings of the IEEE*, vol. 69, no. 3, pp. 349–389, 1981.

[30] D.L. Collins and A.C. Evans, "Animal: validation and application of non-linear registration-based segmentation," *International Journal of Pattern Recognition and Artificial Intelligence*, pp. 1271–1294, December 1997.

[31] T. Gaens, F. Maes, D. Vandermeulen, and P. Suetens, "Non-rigid Multimodal Image Registration Using Mutual Information," in *First International Conference on Medical Image Computing and Computer-Assisted Intervention, MICCAI'98*, W.M. Wells, A. Colchester, and S.L. Delp, Eds., Boston, USA, October 1998, vol. 1496 of *Lecture Notes in Computer Science*, pp. 1099–1106, Springer.

[32] S. Ourselin, A. Roche, G. Subsol, X. Pennec, and N. Ayache, "Reconstructing a 3D Structure from Serial Histological Sections," *Image and Vision Computing*, vol. 19, no. 1-2, pp. 25–31, January 2001, Electronic version: http://www.inria.fr/RRRT/RR-3595.html.

[33] S. Ourselin, A. Roche, S. Prima, and N. Ayache, "Block Matching: a General Framework to Improve Robustness of Rigid Registration of Medical Images," in *Third International Conference on Medical Image Computing and Computer-Assisted Intervention, MICCAI'2000*, S.L. Delp, A.M. DiGioia, and B. Jaramaz, Eds., Pittsburgh, USA, October 2000, vol. 1935 of *Lecture Notes in Computer Science*, pp. 557–566, Springer.

[34] L.G. Brown, "A survey of image registration techniques," *ACM Computing Surveys*, vol. 24, no. 4, pp. 325–375, December 1992.

[35] A. Roche, G. Malandain, X. Pennec, and N. Ayache, "The Correlation Ratio as a New Similarity Measure for Multimodal Image Registration," in *First International Conference on Medical Image Computing and Computer-Assisted Intervention, MICCAI'98*, W.M. Wells, A. Colchester, and S.L. Delp, Eds., Boston, USA, October 1998, vol. 1496 of *Lecture Notes in Computer Science*, pp. 1115–1124, Springer, Electronic version: http://www.inria.fr/RRRT/RR-3378.html.

[36] W.M. Wells III, P. Viola, H. Atsumi, S. Nakajima, and R. Kikinis, "Multi-modal volume registration by maximization of mutual information," in *Medical Image Analysis*. March 1996, vol. 1, pp. 35–51, Oxford University Press.

[37] F. Maes, A. Collignon, Vandermeulen. D., G. Marchal, and P. Suetens, "Multimodality Image Registration by Maximization of Mutual Information," *IEEE Transactions on Medical Imaging*, vol. 16, no. 2, pp. 187–198, Apr. 1997.

[38] A. Roche, G. Malandain, and N. Ayache, "Unifying Maximum Likelihood Approaches in Medical Image Registration," *International Journal of Imaging Systems and Technology: Special Issue on 3D Imaging*, vol. 11, pp. 71–80, 2000.

[39] P.J. Rousseeuw and K. Van Driessen, "Computing LTS Regression for Large Data Sets," Tech. Rep., Statistics Group, University of Antwerp, 1999.

[40] J. West and al., "Comparison and evaluation of retrospective intermodality brain image registration techniques," *Journal of Computer Assisted Tomography*, vol. 21, pp. 554–566, 1997.

[41] N. Roberts, S. Prima, J.-P. Thirion, G. Subsol, and G.H. Whitehouse, "The application of MRI and a new image analysis technique to measure cerebral white matter in healthy young subjects and its sexual dimorphism," in *4th Annual Meeting of the British Chapter of the ISMRM*, Nottingham, UK, December 1998.

[42] T. Barrick, S. Prima, N. Ayache, G.H. Whitehouse, and N. Roberts, "SPM comparison of 3D cerebral asymmetry maps computed for healthy young males and females," in *Fifth International Conference on Functional Mapping of the Human Brain, HBM'99*, Düsseldorf, Germany, June 1999.

[43] S. Ourselin, *Recalage d'images médicales par appariement de régions. Application à la construction d'atlas histologiques 3D*, Ph.D. thesis, Université de Nice, Sophia-Antipolis, January 2002.